Summer 7-15-2018

Pulse Sharpening Circuit for Explosive Emission Cathode Driver

Nicholas D. Kallas
University of New Mexico

Recommended Citation

Kallas, Nicholas D.. "Pulse Sharpening Circuit for Explosive Emission Cathode Driver." (2018). https://digitalrepository.unm.edu/ece_etds/433

Nicholas Kallas

Candidate

ECE

Department

This thesis is approved, and it is acceptable in quality and form for publication:

Approved by the Thesis Committee:

Edl Schamiloglu, Chairperson

Sandra Biedron

Brian McCuistian

Pulse Sharpening Circuit for Explosive Emission Cathode Driver

by

Nicholas D. Kallas

B.S., Electrical Engineering, New Mexico Institute of Mining and Technology, December 2013

THESIS

Submitted in Partial Fulfillment of the
Requirements for the Degree of

Master of Science
Electrical Engineering

The University of New Mexico

Albuquerque, New Mexico

July, 2018

Pulse Sharpening Circuit for Explosive Emission Cathode Driver

by

Nicholas D. Kallas

B.S., Electrical Engineering, New Mexico Institute of Mining and Technology, December 2013

M.S., Electrical Engineering, University of New Mexico, 2018

Abstract

Explosive field emission cathodes (EEC), used for the generation of relativistic electron beams, require short rise-time high-voltage pulses in order to minimize the extraction of off-energy electrons. To this end, a rise-time sharpening circuit has been developed at the Los Alamos National Laboratory (LANL). The circuit consists of a 7 nF water-filled peaking capacitor with an integrated self-breakdown switch designed to operate up to -300 kV. This unit is intended to reduce the rise-time of a 4-stage Type-E PFN Marx Generator that will be used to study operational characteristics of velvet cathodes. Simulations of the peaking circuit show a reduction in voltage rise-time from over 100 ns to roughly 20 ns. Experimental results taken at $\sim$150 kV load voltage showed a reduction in rise-time from 98 ns to 16 ns. This thesis details the simulation, design, and testing of the peaking circuit.

Contents

List of Figures

List of Tables

Chapter 1

Introduction

High current electron beams are typically generated by either the use of large-area or high-current-density cathodes. Explosive emission cathodes serve as one such high current density source of electrons in applications such as electron induction accelerators [1], pumping of excimer lasers [2], free electron lasers [2], and high power microwave (HPM) tubes [3]. In particular, velvet cathodes provide high current densities, do not require external heating, and are inexpensive. In most cases these cathodes consist of a piece of ordinary polymer velvet clamped, or adhered, to a metal plate with a conductive adhesive [1]. Compared to similar cathode technologies, velvet allows for the extraction of high current densities at comparable fields. Thus velvet cathodes have been used in many induction accelerators for the last two dozen years [4]. However, the performance of these cathodes is largely dependent on the quality of the applied voltage pulse from the driving system.

1.1 Velvet Cathode Operation

Velvet cathodes operate via explosive field emission from microscopic fibers that are uniformly distributed over the cathode surface. When the field at the tip of an individual fiber reaches 10s of kV/cm, field emission current heats the fibers, causing them to explosively evaporate material and release surface contaminants such as water vapor, vacuum pump oil, and fiber material [2]. This process leads to the ionization of these contaminants and the development of a predominantly hydrogen plasma column on the cathode surface. The plasma then expands axially and radially into the anode-cathode (A-K) gap via resistive heating [5]. This plasma serves as a space-charge-limited source of electrons that are accelerated across the gap and, in the case of induction accelerators, through a hollow anode into focusing and accelerating elements. This surface flashover process can be observed in Figure 1.1 for the cathode used in the Axis-I injector of the Dual Axis Radiographic Hydrodynamic Test facility (DARHT) [6]. The image series in Figure 1.1 shows 10 ns gates of the cathode light intensity through the evolution of the diode extraction pulse. These images are taken 30° off-axis causing an elliptical appearance of the cathode plasma.

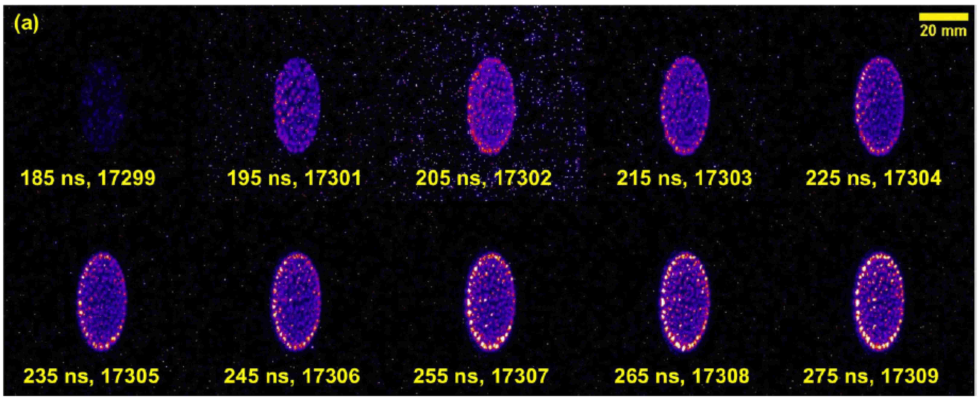

Figure 1.1: The evolution of light intensity from the DARHT Axis-I cathode plasma [6].

Many institutions have performed research on velvet and other cold cathode technologies over the past three decades, but one of the most extensive reviews of velvet cathodes was conducted by the Air Force Research Laboratory (AFRL) [7]. The AFRL researchers studied the performance of cold cathodes for use in HPM devices under different operating conditions such as applied field, pulse repetition rate, and vacuum pumping speeds. The technologies they considered included polymer velvet of the type employed on DARHT Axis-I, carbon fiber, and cesium iodide (CsI) coated carbon fiber, in the interest of improving the performance of their existing systems that employed polymer velvet cathodes. The primary issues they sought to address were pulse shortening of the HPM source due to gap closure from the cathode plasma, high out-gassing, and low cathode lifetime on the order of hundreds to thousands of shots. Comparing the performance of the polymer velvet cathodes, to carbon fiber cathodes with and without CsI coatings in a relativistic magnetron, the CsI-coated carbon fiber cathodes showed significantly reduced impedance collapse and much longer pulse operation. However, the polymer and uncoated carbon velvet cathodes were severely damaged by ion back bombardment, reducing their lifetime. Through their research effort, the AFRL researchers determined that one of the main flaws of velvet cathodes was the introduction of surface contaminants during manufacturing and although this could be significantly improved by careful processing techniques, gap closure remained a major issue.

In many cathode applications, it is important to produce high quality electron beams with narrow electron energy spread. The injection of off-energy electrons into accelerating cells, steering elements, or HPM devices degrades their performance and increases beam emittance. Although the beam is relativistic in many of these cases, lower energy electrons will deflect more in focusing and steering elements causing a number of issues [4].

When electrons enter solenoidal steering elements, the beam will never be perfectly on-axis with the magnetic field causing the electrons to travel along the magnetic field lines inside the solenoid as seen in Figure 1.2. This magnetic field causes the incoming beam to rotate around the magnetic flux lines in the transverse plane. Transverse motion occurs even when the beam and magnets are aligned with respect to the machine axis [1]. If the incoming beam has uniform energy it begins to rotate at the same cyclotron frequency in the transverse plane via the Lorentz force. When chromatic aberrations exist in the beam energy, particles with different energies experience different cyclotron frequencies while passing through solenoidal focusing elements. A difference in cyclotron frequencies causes portions of the beam to experience phase advancement, and the beam no longer rotates as a solid body in the transverse plane. This causes the beam to develop a helical shape. When this phase advancement reaches 2π, the beam displacement over the pulse causes the beam to resemble a corkscrew; hence this transverse motion caused by electron

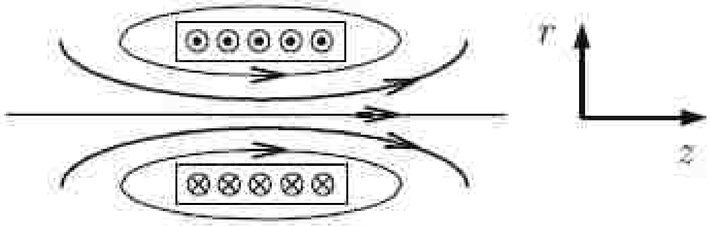

Figure 1.2: Diagram of a solenoid magnet showing magnetic field lines from [1].

energy spread is called corkscrew motion [1].

To generate beams with a narrow energy spectrum, it is important to drive velvet cathodes with a short rise-time, low-ripple voltage pulse. The changing electric field in the A-K gap during the rise and fall times of the driving voltage pulse creates off energy electrons, and this broadens the beam energy during the these transitions. Electrons emitted during the voltage transitions will be injected into the accelerating and focusing elements with a broad range of energies. This issue is compounded by the relatively high source temperature of velvet cathodes, which causes higher transverse beam emittance.

In addition to degrading the quality of the electron beam, a portion of the off-energy electrons will be deflected to such a degree that it either scrapes the beam tube or narrowly passes through the anode and gets over-focused further down-stream [5]. Since most accelerator beam pipes are made of stainless steel, this scraping generates Bremsstrahlung with the same energy spectrum as the electrons hitting the beam pipe. This was shown by J. Coleman at the DARHT I accelerator facility [5], where pulses of X-ray energy were measured around the beam pipe during the head and tail of the beam pulse.

1.2 Pulse Sharpening

Because of the issues created by off energy electrons during the transitions of the cathode voltage pulse, it is important to develop pulsed power systems that generate high-quality driving pulses with short rise and fall times. The necessity of high quality voltage pulses is not unique to this application, and there exists a number of techniques to improve the rise and fall times of pulsed power systems. Pulse sharpening can be achieved through the use of peaking switches, magnetic flux compression, capacitive ladder circuits, and non-linear transmission lines among others. One of the most simple and robust topologies among these for rise-time sharpening is the peaking capacitor circuit. A peaking circuit consists only of a shunt capacitor and series switch placed between the pulsed power source and load.

1.3 Organization of this Thesis

This thesis describes the design methodology and testing results for a pulse rise-time-sharpening circuit developed in support of a cathode test stand for the DARHT facility at Los Alamos National Laboratory. The circuit consists of a 7.8 nF water-filled peaking capacitor with an integrated self-breakdown switch designed to operate up to -300 kV. The unit is intended to reduce the rise-time of a PFN Marx generator as part of a cold-cathode testing fixture that is currently under development.

The remainder of this thesis is organized as follows. Chapter 2 presents an overview of the cathode test stand being assembled at LANL. Chapter 3 describes the design process and construction of the peaking circuit. Chapter 4 presents a summary of the experimental results. Chapter 5 discusses shortcomings of the unit discovered during testing, future improvements, and conclusions. Additional technical information is presented in the three Appendices.

Chapter 2

Cathode Test Stand

The necessity for multi-pulse radiography systems has created the need for a new generation of induction accelerators with more demanding operational requirements. Among other issues, such as induction cell design and insulator flashover, the effects of multiple pulses on present cathode technologies are poorly understood and have only been demonstrated in a select number of specific applications [5] [8]. In the case of explosive emission cathodes, there are issues such as gap closure and cathode lifetime [2] that need to be thoroughly evaluated before this technology can be used in each specific application. In order to investigate the viability of multi-pulse cold cathode technologies for the DARHT accelerators, a Cathode Test Stand (CTS) is being developed at LANL.

The CTS will consist of a reconfigurable vacuum enclosure containing the A-K gap with a solid anode design. The high-voltage driving pulse will be generated by a

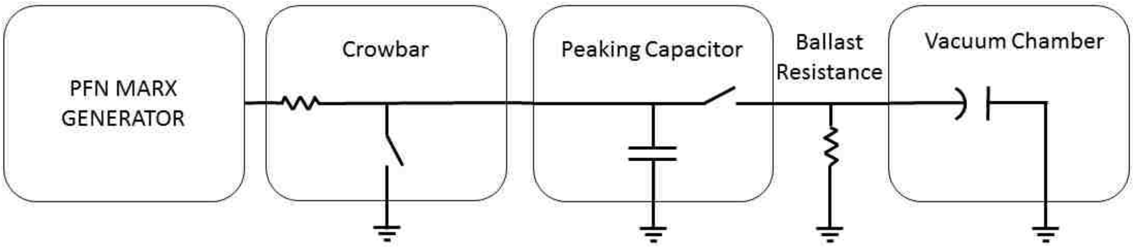

Figure 2.1: System level configuration of the cathode test stand under development at LANL.

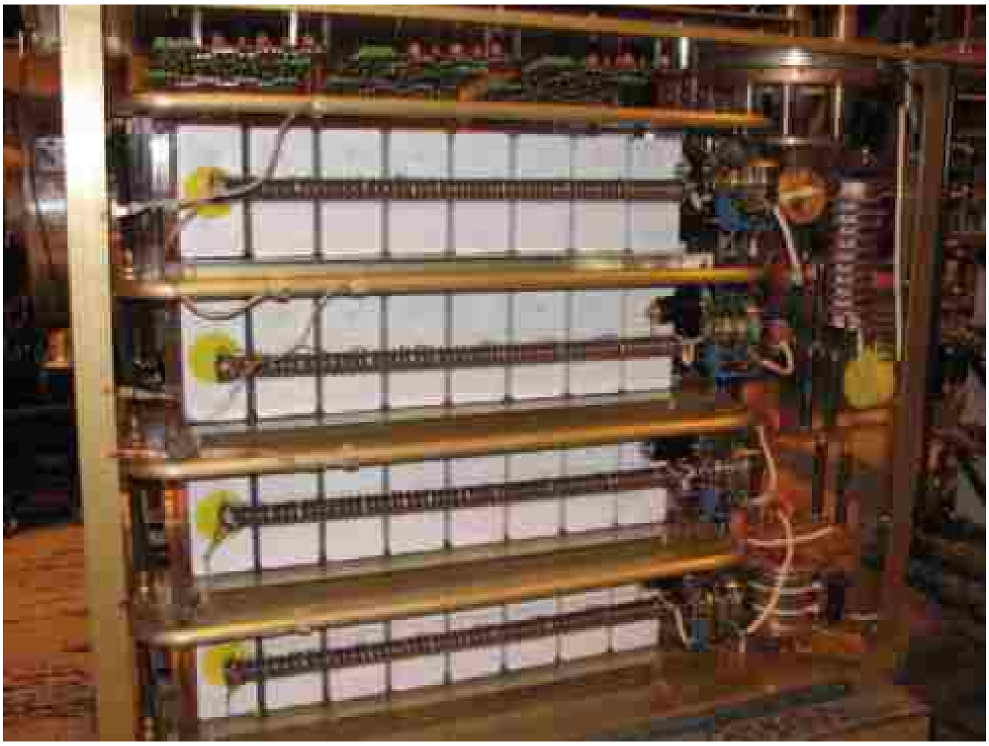

Figure 2.2: PFN Marx generator used to drive the DARHT Axis-II induction cells [9].

4-stage PFN Marx generator connected in series with a crowbar circuit and peaking capacitor as shown in Figure 2.1. The PFN Marx is the same design as that used on DARHT Axis-II to drive the accelerator induction cells [9]. The pulser consists of a 7-section, Type-E, 4-stage unipolar PFN Marx unit as shown in Figure 2.2. This unit produces a 2 μs pulse of up to $-350\,\text{kV}$ into a $\sim 22\,\Omega$ load with a rise-time of approximately 150 ns [9]. The external addition of the crowbar circuit allows for both a faster fall-time and variable pulse width, while the peaking capacitor described herein showed a reduction in PFN Marx rise-time to between $14 - 19\,\text{ns}$.

By developing a test stand that can drive cold cathodes with variable pulse widths and amplitudes, the viability of different cathode materials can be assessed for a variety of different operational conditions. In addition, the vacuum enclosure can be reconfigured to accommodate a large range of cathode sizes and A-K gap spacings as well as a variety of different diagnostics. The emission characteristics of velvet under long pulse conditions ($1-2\,\mu$s) are of particular interest for potential use with the DARHT II injector. There is also the potential for upgrading the CTS to test velvet under multipulse conditions in order to investigate the possibility of future multipulse capabilities on the DARHT I accelerator.

In this chapter, the need for flexible cathode testing capabilities were discussed and the proposed cathode test stand was introduced. As part of this cathode test stand a peaking capacitor is being developed to shorten the rise-time of the voltage pulse generated by a PFN Marx generator in order to provide high-quality pulses of up to -300 kV to an A-K gap. In Chapter 3 the design methodology for the peaking capacitor is laid out and a set of physical parameters are defined. These parameters were determined with the assistance of electrostatic FEA and SPICE simulations, and the results are presented.

Chapter 3

Design

3.1 Introduction

As discussed in Section 1.1, it is important to minimize the rise and fall times of the applied voltage on cold cathodes. Ideally making rise-time at least an order of magnitude shorter than the duration of the applied pulse is necessary. Since the shortest pulse widths of interest are on the order of 100 ns for the CTS it is desirable to have a voltage rise-time of less than 20 ns. It is for this reason that a peaking capacitor circuit is being developed for use on the CTS. Peaking capacitors operate by storing a portion of the energy of the rising edge of an incoming pulse and discharging at some point prior to the pulse reaching full voltage. This effectively shunts the inductance of the pulse generator, creating a sharper rise-time on the output pulse.

The optimal capacitance for a peaking circuit is based on the total energy contained in the rise-time portion of the pulse. This is determined by integrating the product of the voltage and current (power) waveforms over the rise-time to determine the total energy as

$$U = \int_0^{\tau} i(t)v(t)dt. \tag{3.1}$$

The capacitance required to store this energy can then be determined from

$$C = \frac{2U}{V_{max}^2}. \tag{3.2}$$

Using these equations for the PFN Marx unit with a peak (maximum amplitude) output voltage of −300 kV (V_{max}), the required capacitance is 18 nF. In reality only a portion of this energy needs to be stored in order to achieve significant pulse sharpening. The capacitance of the peaking circuit, combined with its parasitic inductance, primarily defines the final rise-time of the pulse; thus it is important to keep these values as small as possible. Because this device will use a water dielectric and operates at 100s of kilovolts, reducing the required capacitance has the additional advantage of significantly reducing its physical size.

3.2 SPICE Simulations

In order to accurately characterize the addition of a peaking capacitor to the PFN output, a detailed model of the Axis-II Marx circuit (Figure 3.1) was developed. First, a single, 7-section Type-E circuit was established, then expanded to replicate the behavior of the 4-stage PFN Marx. Diagnostic circuits were added in order to make the measured signals from the SPICE simulations match the experimental results as closely as possible. Using this method, the Axis-II Marx was satisfactorily modeled in LTspice and this model was used to select a value for the peaking capacitor as will be seen in the following sections.

Although an estimate of the needed peaking capacitance was determined in the previous section, the minimum value required to achieve pulse sharpening will only be some fraction of this. The reduction in capacitance is necessary because the peaking switch needs to be fully conducting prior to the capacitor reaching peak PFN voltage; furthermore, there is a significant amount of time, on the order or several nanoseconds, between switch breakdown initiation and full conductance, reducing the required amount of stored energy to the portion of the rising pulse prior to switch

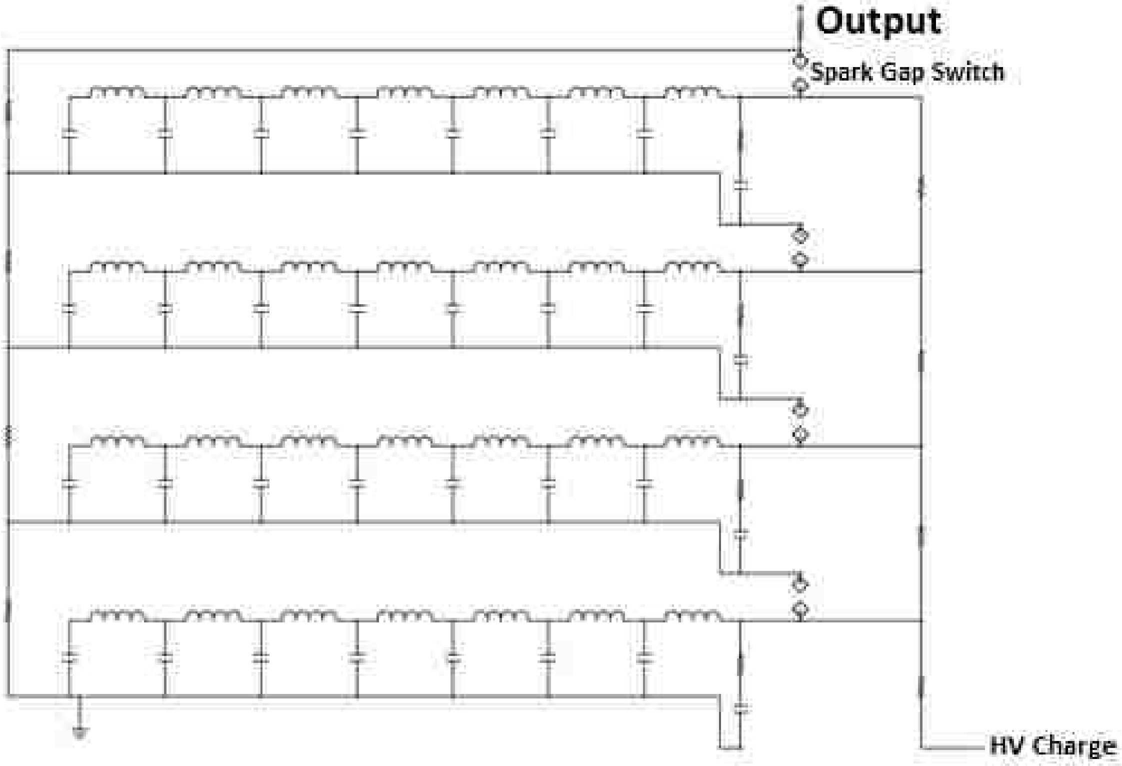

Figure 3.1: Circuit diagram of the PFN Marx generator.

closure. This value was determined by establishing a model with the calculated peaking capacitor value and reducing the capacitance until the best performance was obtained.

3.2.1 Type-E PFN

Based on models previously created by Michael Kang of LANL [10], a single Type-E PFN was developed in SPICE, shown in Figure 3.2, to replicate the top stage of the PFN Marx generators that drive the induction cells on DARHT Axis-II. To match the impedance of the actual system, the capacitance was set to 40 nF per section and the inductance values were set to achieve a $\sim 22\,\Omega$ characteristic impedance. The PFN impedance is intended to match the output impedance of the four parallel, $70\,\Omega$ cables used to drive the induction cells of DARHT Axis-II. The values of the stage inductors were set to 504, 633, 779, 942, 942, 2032 nH, respectively, based

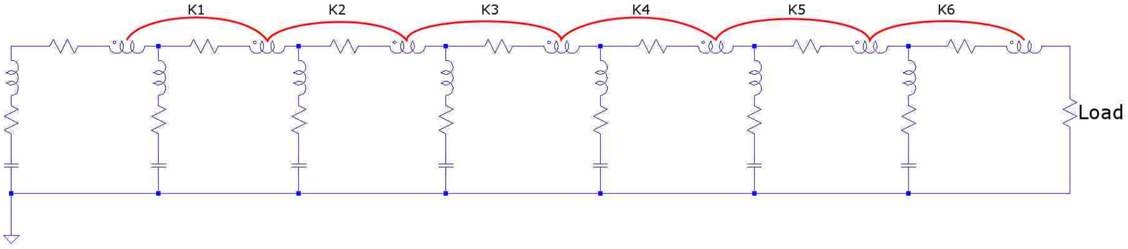

Figure 3.2: Circuit diagram of a 7-Stage Type-E PFN with parasitic elements.

on a Type-E PFN topology with a 1.8 μs flat top and 22 Ω impedance, tuned to compensate for voltage droop and beam loading on the induction cells. Likewise, the coupling coefficients between the inductors of stages 1-7 were set to 0.051, 0.055, 0.058, 0.059, 0.059, and 0.063, respectively. The values of capacitor series inductance and resistance, and inductor resistance were estimated to be roughly 100 nH, 20 mΩ, and 14 mΩ based on finite element analysis previously done by Kang. For simplicity, the circuit in Figure 3.2 uses initial conditions rather than a charging supply and output switch. The use of initial conditions makes the effective time of switch closure occur at the beginning of the simulation, as seen in Figure 3.3.

Charging the single PFN to 100 kV, the peak output voltage is 84.55 kV, with

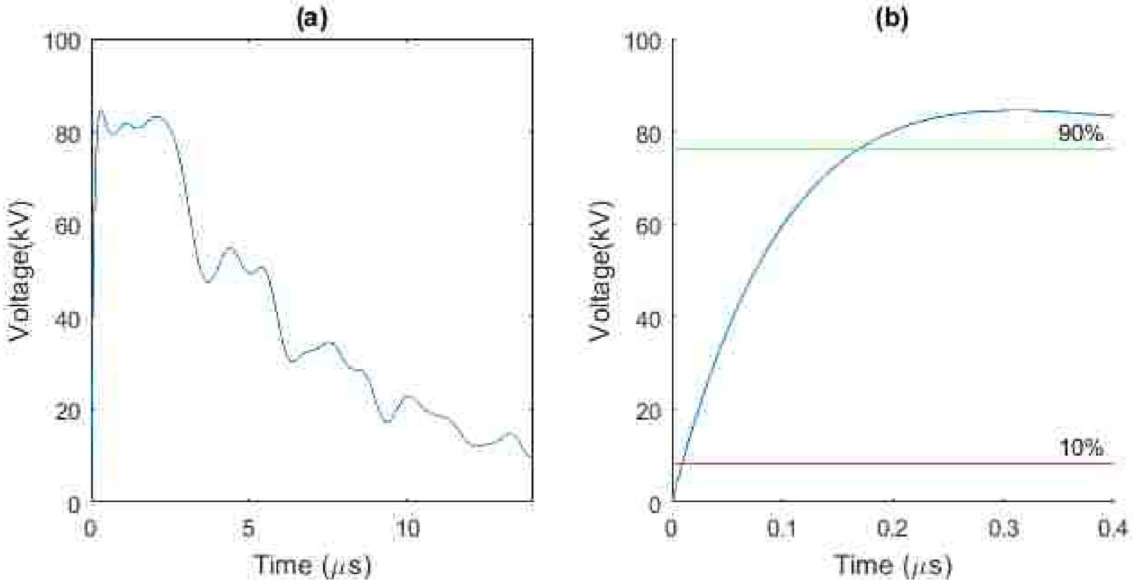

Figure 3.3: The load voltage is shown for the circuit depicted in Figure 3.2 with 100 kV charge in (a), and a detailed view of the rising edge in (b).

$\sim 6\,\%$ flat top ripple, and the $10-90\,\%$ rise-time is 160 ns as seen in Figure 3.3 (a), which closely matches the measured rise-time of $150\,\mu$s [11]. The peak voltage and current at the output are 84.5 kV and 3.8 kA, with a peak power of 200 MW and a total energy from 0 to 300 ns of 64 J. To store all energy contained in the rising edge of the pulse, Eq. (3.2) gives a required capacitance of 18 nF.

3.2.2 Peaking Capacitor

The next iteration of this simulation included a switch on the output of the PFN representing the field effect spark gap switch employed in the PFN Marx, a 18 nF peaking capacitor, and a self-break spark gap switch on the output (sub-circuit netlist shown in Appendix A). The switch was given a series inductance value of 98 nH, a series resistance of 1 mΩ, and shunt capacitances on the input and output of 88 pF and 50 pF, respectively. These values were taken from the Kang simulation of the switches. The output switch uses a self-break spark gap model based on back to back diodes and a series variable resistor that controls breakdown threshold. In addition, the output spark gap has a series inductance of 73 nH, and 50 pF output capacitance. This circuit is shown in Figure 3.4.

Figure 3.5 shows that the addition of a peaking capacitor to the PFN model

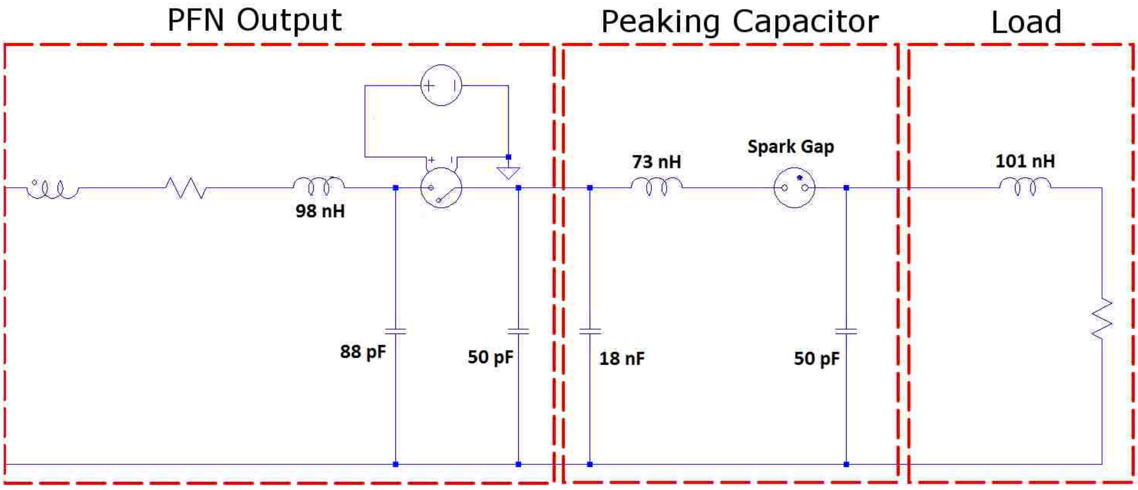

Figure 3.4: The Type-E PFN circuit with a peaking capacitor and 22 Ω load.

contributed some rise-time sharpening; however, the pulse shape is significantly degraded as compared to the PFN output with no peaking capacitor circuit. It is also evident from the higher peak voltage that the capacitor is experiencing resonant charging even after switch closure.

A new value for the peaking capacitor was selected by starting with 18 nF (previously calculated) and reducing the capacitance until the approximate optimal value was found to be 5 nF. This value provided a sharper rising edge without significant voltage overshoot caused by resonant charging. The flat-top of the output pulse appears to be appreciably degraded, but the effects of this voltage variation on a velvet cathode load are yet to be investigated. The voltage threshold of the self-break spark gap switch was adjusted accordingly. Prior to the physical design of the capacitor it is difficult to approximate its series inductance so this value was neglected for this circuit, but is addressed in later sections. The output of the circuit from Figure 3.4 with a 5 nF peaking capacitance is shown in Figure 3.6 and it is clear that the performance is markedly improved over Figure 3.5. With the addition of a 5 nF peaking

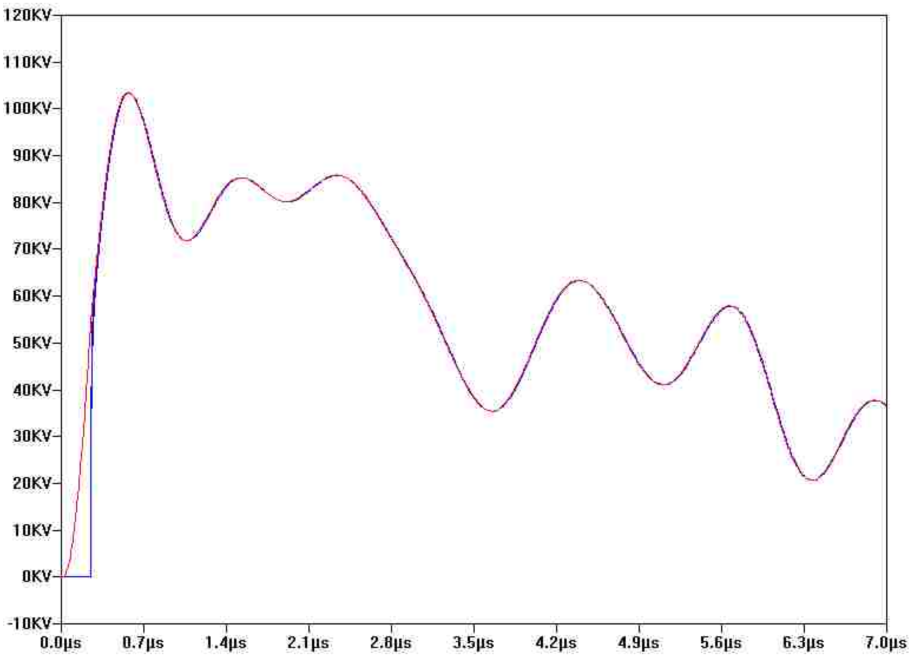

Figure 3.5: These waveforms show the voltage across the load resistor (blue) and peaking capacitor (red) for the circuit shown in Figure 3.4.

capacitor the rise-time of the single 7-stage Type-E PFN was reduced from 160 ns (Figure 3.3) to approximately 60 ns (Figure 3.6). As will be seen in Section 3.2.4 this capacitance does not scale with the addition of stages for the PFN Marx due to the difference in stored energy.

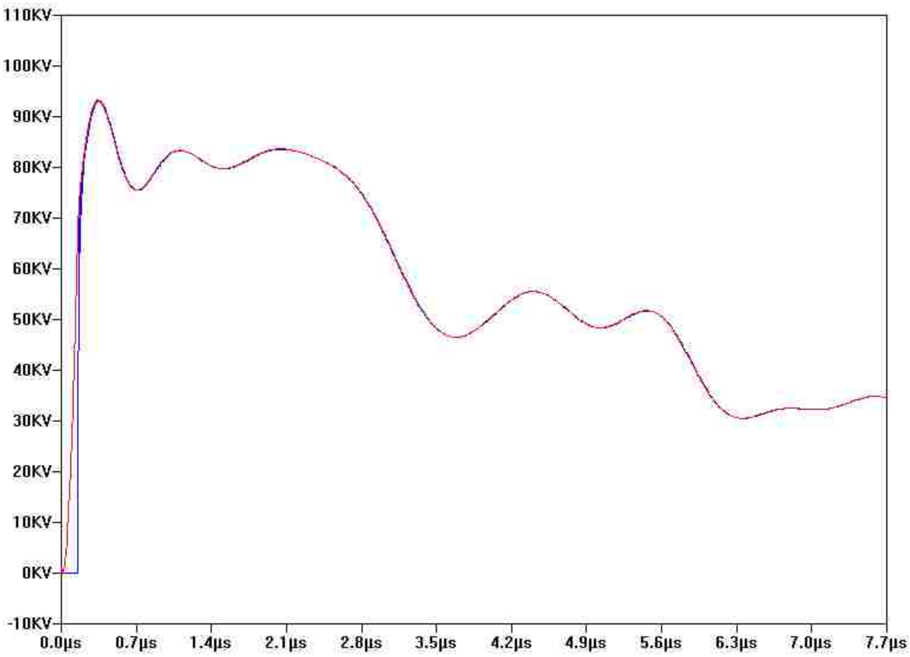

Figure 3.6: These waveforms show the voltage across the load resistor (blue) and peaking capacitor (red) for the circuit in Figure 3.4 with a 5−nF peaking capacitance.

3.2.3 Peaking Capacitor Dimensions

To determine the physical size of the peaking capacitor and estimate the series inductance introduced into the circuit, the geometry and dielectric characteristics must be taken into account. For the purpose of this application, it is preferable to use a capacitor that does not require a solid dielectric. Deionized water was chosen for this design due to its high voltage hold-off over microsecond time scales [12] and high dielectric constant ($\epsilon_{\mathrm{r}} = 80$) compared to Shell Diala oil or sulfur hexafluoride ($\mathrm{SF_6}$). Because of the fixed geometry of the peaking capacitor, water also offers the additional advantage of tunability with dielectric constant by the addition of glycol. The compatibility with glycol allows for the adjustment of the relative permittivity from 80.4 (100% water) to 37 (100% glycol) [13], allowing for a 54% variability in total capacitance. The ability to reduce the capacitance with the addition of glycol offers the adjustability of the rise-time on the output pulse. The characteristics of the capacitor are listed in Table 3.1.

Table 3.1: Capacitor specifications based on the results of Section 3.2.2.

Capacitance (C)	Voltage ($\mathrm{V_{MAX}}$)	Pulse Width (τ)	Permittivity (ϵ_{r})	Length (l)
10 nF	−350 kV	3.5 μs	80	12 inches

For simplicity in construction and mitigation of electric field enhancements, a coaxial capacitor scheme is used. In order to determine the dimensions of a coaxial capacitor with the specifications given in Table 3.1, Eq. (3.3) can be used to determine the ratio of the outer radius of the coax (b) to the radius of the inner conductor (a). For a given length, the optimal dimensions can then be determined by calculating the breakdown field based on the chosen ratio [13]. The capacitance per unit length is given by

$$\frac{\mathrm{C}}{\mathrm{l}} = \frac{2\pi\epsilon_{\mathrm{o}}\epsilon_{\mathrm{r}}}{\ln(\frac{\mathrm{a}}{\mathrm{b}})}, \tag{3.3}$$

which can be rearranged to give the ratio of the outer and inner diameters by

$$\frac{\mathrm{b}}{\mathrm{a}} = \exp\Big(\frac{2\pi\epsilon_{\mathrm{r}}\epsilon_{\mathrm{o}}\mathrm{l}}{\mathrm{C}}\Big). \tag{3.4}$$

In order to determine the voltage at which the coaxial structure will experience breakdown, the field enhancement of the structure must be taken into account. Eq. (3.6) shows the maximum electric field $\mathrm{E_{Max}}$ created by an applied voltage $\Delta\mathrm{V}$ for a coaxial structure [14]. This equation can be rearranged in order to determine the minimum radius for a given voltage and maximum electric field, given by

$$\mathrm{a_{min}} = \frac{\Delta\mathrm{V}}{\mathrm{E_{Max}}\ln(\frac{\mathrm{b}}{\mathrm{a}})} \tag{3.5}$$

$$\mathrm{E_{Max}} = \frac{\Delta\mathrm{V}}{\mathrm{a}[\ln(\frac{\mathrm{b}}{\mathrm{a}})]}. \tag{3.6}$$

Next, a relation between the peak electric field and the dielectric breakdown strength of deionized water must be established. This can be done using J.C. Martins semi-empirical equation for static breakdown threshold of dielectrics, given by [12]

$$\mathrm{k_{\pm}} = \mathrm{E_{Max}} \cdot \tau^{1/3} \cdot \mathrm{A}^{1/10}, \tag{3.7}$$

where τ is the effective duration of the applied voltage in seconds, A is the area of the conductor under field stress in cm^2, and $\mathrm{k_{\pm}}$ is an experimentally determined constant that is defined by the chosen dielectric and polarity of the applied pulse. For the case of deionized water under negative polarity, the constant $\mathrm{k_{\pm}}$ is 0.3 [12].

Combining the results of Eqs. 3.4, 3.5, and 3.7, the minimum radius was numerically determined by varying *a* over a range of physically realizable values for a fixed capacitor length of 1 foot. The resulting peak field intensity and static breakdown threshold were plotted and the minimum radius occurs at the intersection of the curves as displayed in Figure 3.7 for the parameters listed in Table 3.1. In Figure 3.7, IR(a) is the inner radius and OR(b) is the outer radius of the coaxial capacitor.

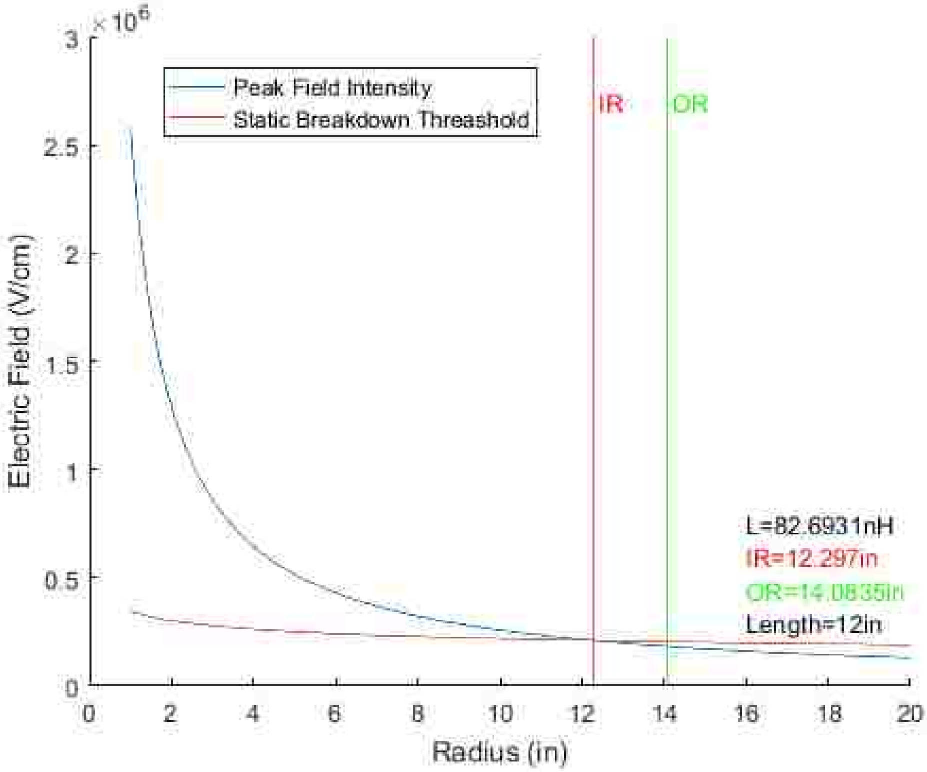

Figure 3.7: Numerical determination of coaxial capacitor parameters for values specified in Table 3.1.

Once the geometry of the capacitor is determined using the above process, the series inductance of the capacitor can be estimated using

$$\mathrm{L} = \frac{\mu}{2\pi} \cdot \ln\left(\frac{\mathrm{b}}{\mathrm{a}}\right)\frac{1}{\mathrm{C}}. \tag{3.8}$$

For the specifications listed in Table 3.1 the parasitic inductance was estimated to be 82.7 nH as shown in Figure 3.7.

3.2.4 DARHT Axis II PFN Marx

The results in Section 3.2.3 are based on the assumption of a single Type-E PFN at 100-kV charge. Using the same method, the results can be expanded to the 4-stage PFN Marx topology shown in Appendix B. For this configuration, a charging supply was required because floating voltages cannot be defined by initial conditions in

LTspice (i.e. voltages cannot be defined between nodes but only relative to ground). The charge voltage per stage was 100 kV which is the maximum charge for the PFN Marx units. The rise-time of the simulated output pulse measured across the 22 Ω load from 10 − 90 % was 280 ns. The output voltage and current waveforms are shown in Figure 3.8. The addition of extra stages increased the rise-time to 280 ns, but reduced the flat-top ripple to 7.5 %. This rise-time is slightly longer than on the PFN units; however, this output closely matches that of the actual system.

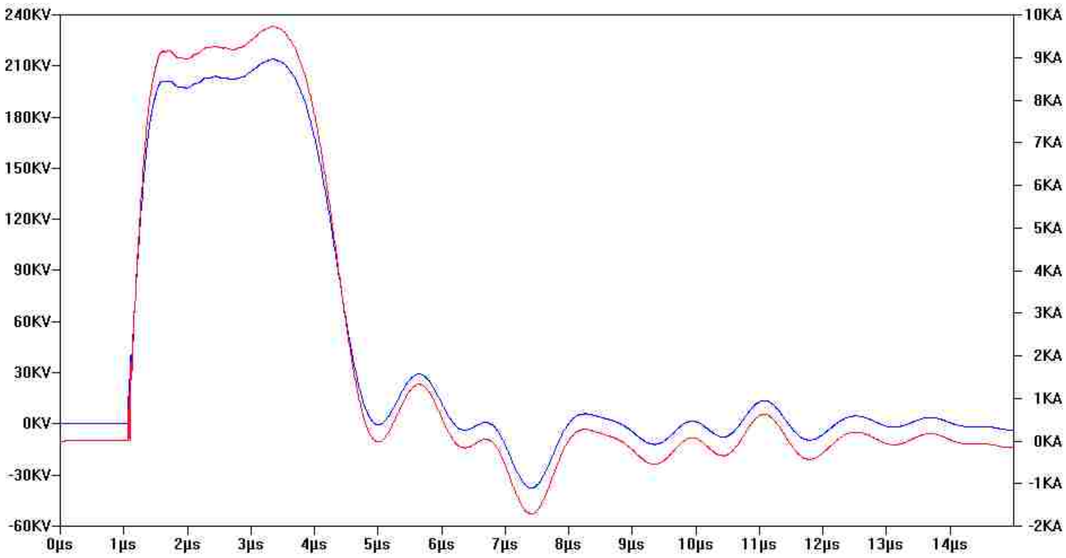

Figure 3.8: Load voltage (blue) and current (red) for the circuit depicted in Appendix B with 100 kV charge.

A comparison of the simulated waveform and the measured data for a 44 Ω load is shown in Figure 3.9. For the experimental data the voltage was measured using a resistive divider on the PFN dummy load. The rise-time of the simulated pulse with a 44 Ω load is slightly faster than that shown for 22 Ω in Figure 3.3. The mismatched impedance of the 44 Ω load case causes a voltage overshoot that contributes to this faster rise. The difference in transient characteristics of the simulated pulse may appear from under-damped parasitic circuit elements, combined with the limited bandwidth of the measurements in the real circuit. Also note, from Figure 3.9 the simulated data was inverted and scaled to match the negative polarity of the measured pulse. The models were developed with a positive polarity because of intrinsic difficulties of using negative polarity in LTspice for certain applications, the results are otherwise identical.

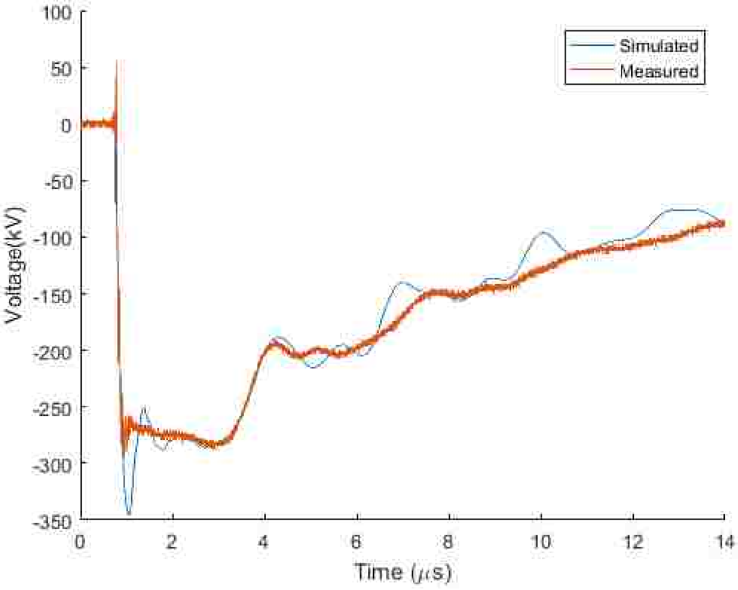

Figure 3.9: Comparison of simulated and experimental data for a 44 Ω load.

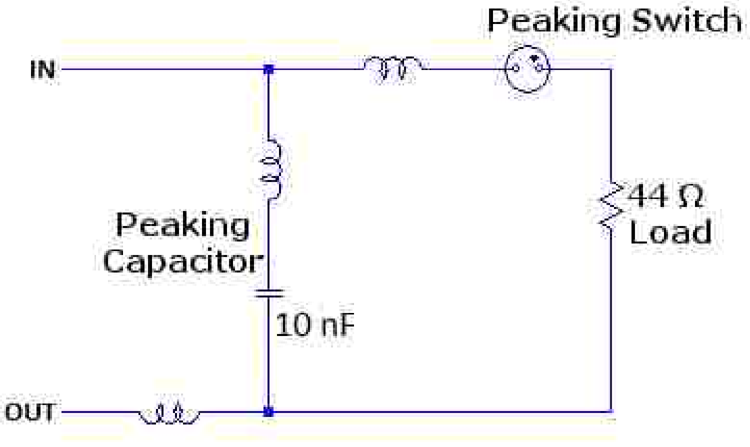

Figure 3.10: Diagram of the simplified peaking capacitor circuit with a 44 Ω load.

Aside from the additional transient characteristics of the simulated data in Figure 3.9, the SPICE model provides a very close approximation to the PFN Marx unit. Next, the peaking capacitor was added to the full circuit. The output configuration was simplified to a 10 nF peaking capacitance with a series inductance and self-break output switch, with a 44 Ω load as seen in Figure 3.10. The inductance of the peaking circuit was estimated to be 84 nH using the physical dimensions of the capacitor that were calculated in section 3.2.3. The peak voltage measured across the load was $-300\,\mathrm{kV}$, lower than the actual output for the $-100\,\mathrm{kV}$ charge. Efficiency per stage in the SPICE model dropped dramatically with the addition of each PFN stage to the Marx. The anomalous drop in voltage was dealt with by scaling the simulated data for comparison to experimental results. This method proved to be adequate in the determination of the peaking capacitance. The measured rise-time of the output pulse for the circuit in Figure 3.10 was $\sim 25\,\mathrm{ns}$ as seen in Figure 3.11. There is also clearly a high-frequency ripple on the rising edge caused by the parasitic inductance of the peaking capacitor.

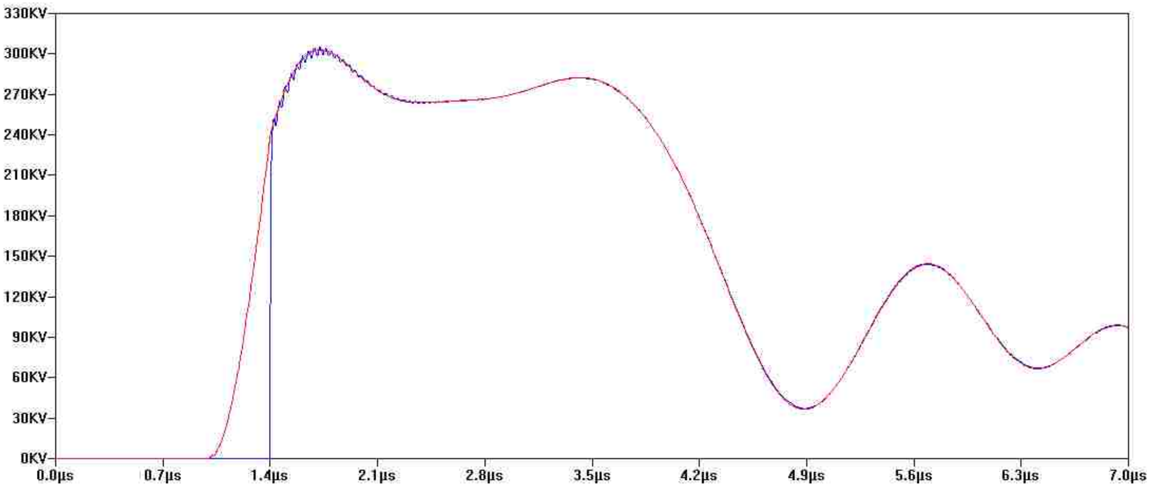

Figure 3.11: These waveforms show the voltage across the load resistor (blue) and peaking capacitor (red) for the circuit in Figure 3.10.

By repeating the process of incrementally decreasing the peaking capacitance from Section 3.2.3, the optimal value was found to be $7.8\,\mathrm{nF}$. This optimal value was determined by observing the point at which the rising voltage overshoot was minimized. Using this new value for the capacitance, the parasitic inductance was estimated to be $106\,\mathrm{nH}$ for similar dimensions as seen in Figure 3.12. The resulting rise-time was reduced to $21\,\mathrm{ns}$ while the voltage overshoot remained roughly the same. Note from the increased inductance that this rise-time can be further reduced by choosing a larger diameter; however, the physical dimensions will be constrained to a maximum of 20 inches in diameter as will be discussed in Section 3.4.

Once the operation of the simplified peaking output circuit model was confirmed,

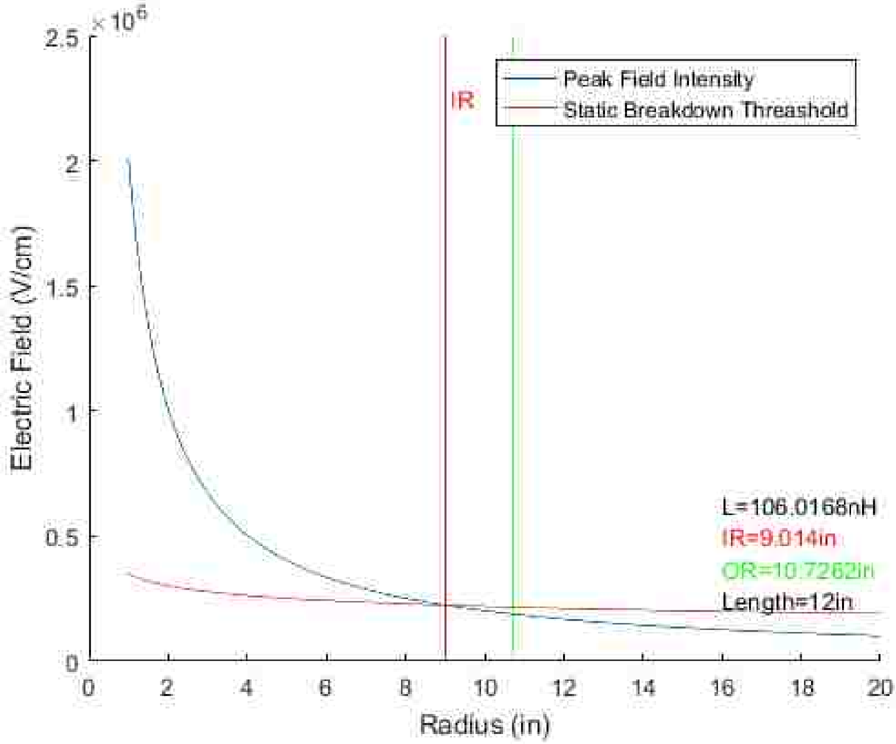

Figure 3.12: Coaxial capacitor parameters for a 7.8 nF capacitor.

it was expanded to include the transmission line that connects the peaking capacitor to the load. Since the CTS did not have space to mount four cables to the cathode vacuum enclosure, the PFN Marx was modified to have a single output cable. The cable feeding the peaking capacitor was ignored in the simulations because its inductance is shunted at the closure of the peaking switch, but the 25 foot section of 70 Ω cable between the peaking capacitor and load was included as seen in Figure 3.14. In addition to the cable, the output capacitance and inductance, 197 pF and 18 nH respectively, of the PFN Marx were included. The resulting output voltage across the 44 Ω load is shown in Figure 3.15 and had a reduction in rise-time to 15 ns. The ripple over the flat-top portion of the pulse was measured to be 5.9 %.

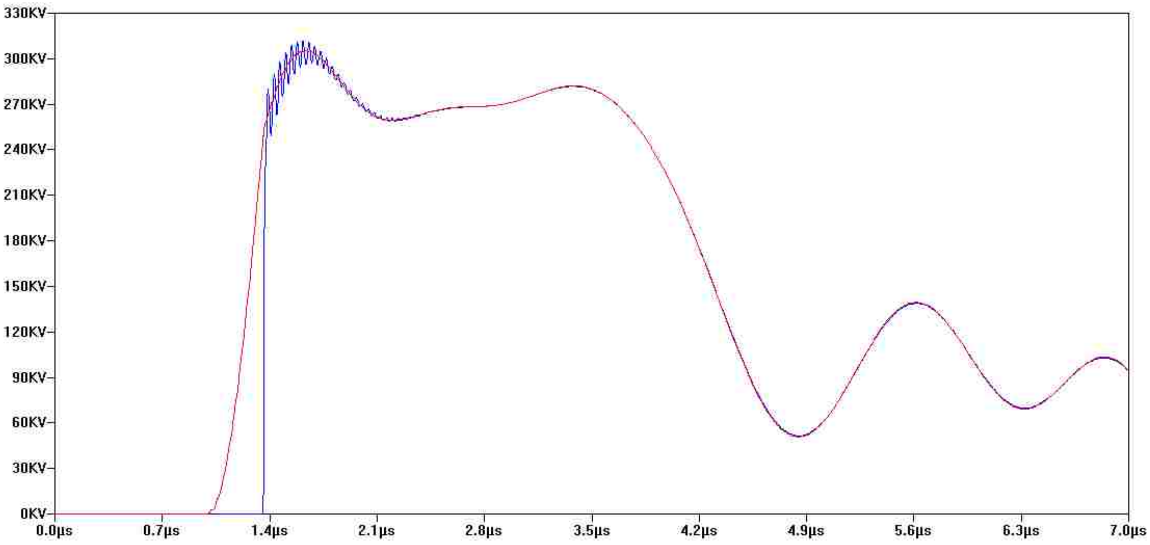

Figure 3.13: These waveforms show the voltage across the load resistor (blue) and peaking capacitor (red) for the circuit in Figure 3.10 with a 7.8 nF peaking capacitance.

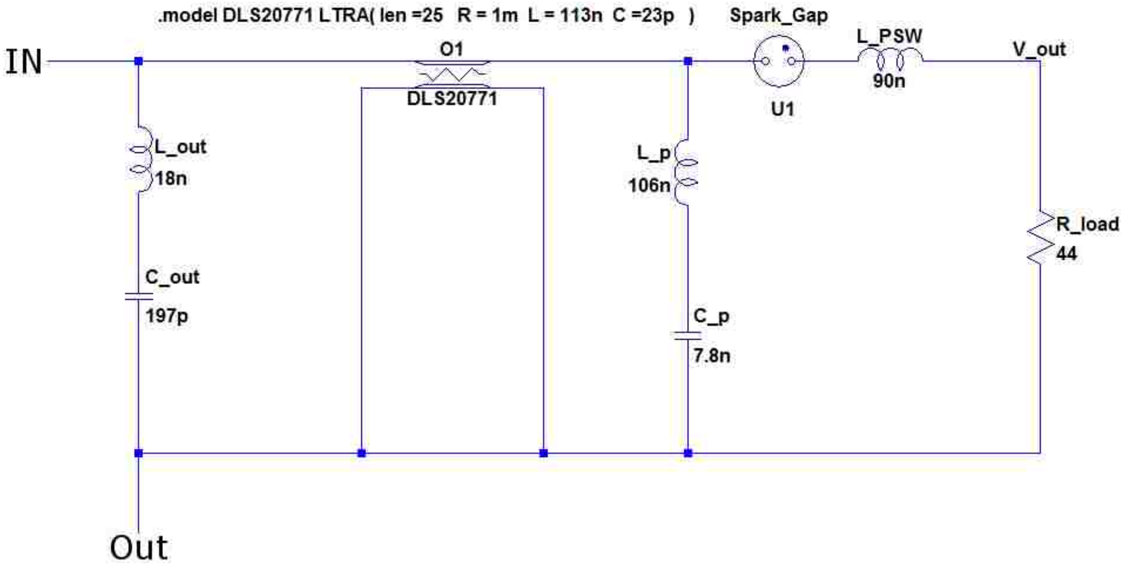

Figure 3.14: Diagram of the peaking circuit for the full PFN Marx simulation with a single output cable.

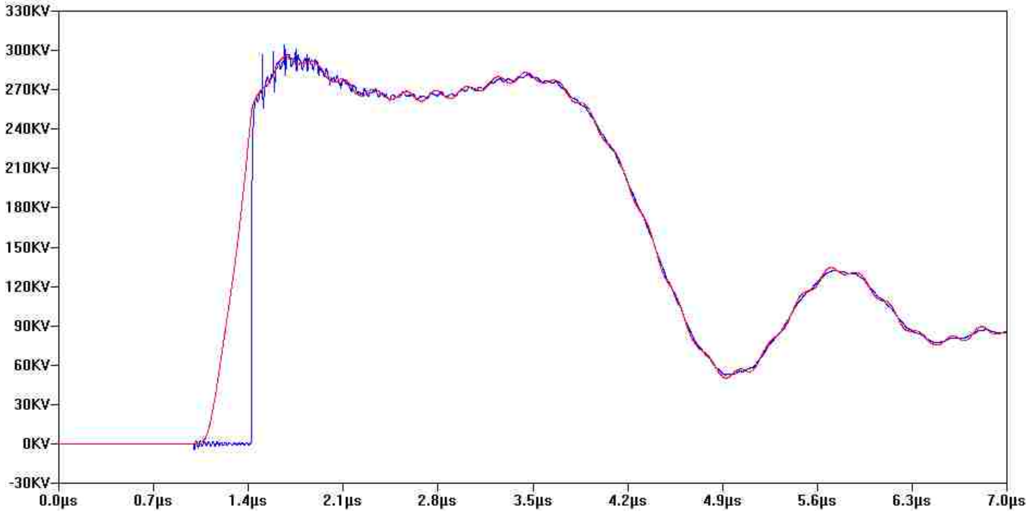

Figure 3.15: These waveforms show the voltage across the load resistor (blue) and peaking capacitor (red) for the circuit in Figure 3.14.

3.3 Diagnostics

To more accurately characterize the peaking circuit in SPICE, diagnostic circuits were added to the model. To measure both the voltage and current of the peaking capacitor, an E-dot probe and Rogowski coil were introduced. These diagnostics circuits were modeled based on their geometry in the implemented peaking capacitor. Using diagnostic models allowed for a more direct comparison of simulated and measured data once the peaking capacitor was tested. Simulation and implementation of these diagnostic devices are discussed in the following sections.

3.3.1 Rogowski Current Monitor

The Rogowski coil is an air-core current transducer that measures both alternating and impulse currents via Ampere's and Faraday's laws [15]. Rogowski coils consist of a conductor wound around an insulator that contains a return current conductor (typically a piece of coaxial cable with the ground braid removed) which is connected at one end to the winding [15]. The Rogowski is placed toroidally around a current path, and the signal is measured between the inner and outer conductors. The voltage is related to the current enclosed by [13]

$$\mathrm{v_0(t)} = \int \vec{\mathrm{B}} \cdot \mathrm{d}\vec{\mathrm{A}} = \frac{\mathrm{A}}{\mathrm{s}}\mu_0 \frac{\mathrm{di(t)}}{\mathrm{dt}} \tag{3.9}$$

where $\mathrm{v_0(t)}$ is the measured voltage signal, A is the winding cross section, and s is the number of turns per unit length. Since the Rogowski is an air core device it has several advantages over other current measurement methods: it does not experience saturation effects, it has linear characteristics, and it can be easily positioned around the current path of interest [16].

In order to implement a Rogowski into the SPICE models presented in previous sections, a lumped model approximation was used. Using a lumped element model allows for the construction of a circuit model that combines the distributed values of

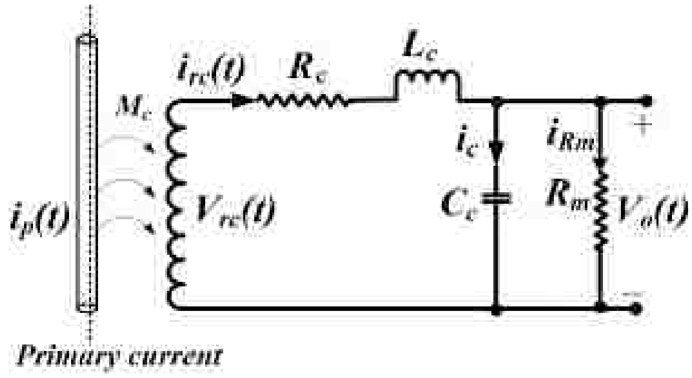

Figure 3.16: Lumped circuit model of a Rogowski coil from [15].

a Rogowski into discrete electrical components as seen in Figure 3.16. These discrete lumped element values can be calculated from

$$\mathrm{R_C} = \rho_\mathrm{c}\frac{\mathrm{l_w}}{\pi \mathrm{d}^2} \tag{3.10}$$

$$\mathrm{L_C} = \frac{\mu_0 \mathrm{N}^2 \mathrm{d_{rc}}}{2\pi}\log\Big(\frac{\mathrm{b}}{\mathrm{a}}\Big) \tag{3.11}$$

$$\mathrm{C_C} = \frac{4\pi^2\epsilon(\mathrm{b}+\mathrm{a})}{\log\Big(\frac{\mathrm{b+a}}{\mathrm{b-a}}\Big)}, \tag{3.12}$$

where ρ_C is the electrical resistivity of the coil wire, l_w is the length of the coil, d is the radius of the wire, d_{rc} is the diameter of the coil loops, N is the number of turns, and a, b are the major and minor radii of the Rogowski [15].

Based on the physical dimensions of the peaking capacitor that are shown in later sections, and a minimum rise-time of 15 ns, a Rogowski coil was ordered from T&M Research Products, Inc. (T&M). From the specifications provided by the manufacturer shown in Table 3.2, a lumped element model was constructed in SPICE from the equations above. The resulting circuit is shown in Figure 3.17. The inductance of the load was estimated to be 10 nH, much lower than that of the actual Rogowski.

Table 3.2: The Rogowski coil specifications provided by T&M.

Max current (kA)	7
di/dt (kA/μs)	5,000
Volts out	80.43
Probe diameter (cm)	0.2921
Probe length (cm)	86.69
Wire diameter (μm)	35.56
Wire resistivity (Ω/cm)	10.63
Minor diameter (cm)	13.34
Probe inductance (nH)	184.3

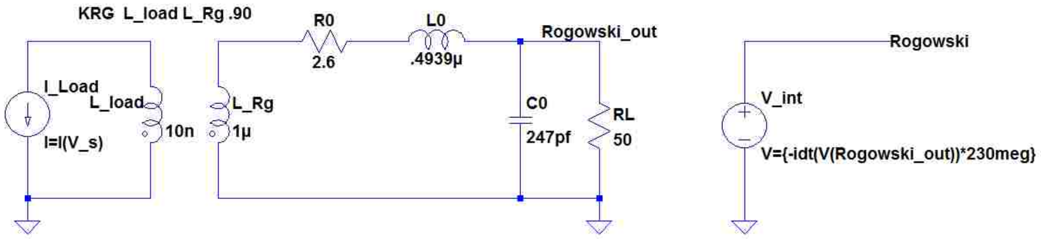

Figure 3.17: Rogowski lumped element model implemented in SPICE.

3.3.2 E-Dot Voltage Probe

E-dot voltage probes are capacitive voltage dividers, consisting of the capacitance between a target conductor and the probe surface (C_H in Figure 3.18), and the capacitance between the probe surface and grounded probe body (C_E from Figure 3.18). E-dot probes provide passive, non-contact measurement of time-varying voltages. An existing E-dot probe design of the type employed on DARHT Axis-I was used for voltage measurement on peaking capacitor [17]. A diagram of the probe is shown in Figure 3.19. It consists of a pick-up "button" (left) connected to the center pin of an HN-type connector (right), insulated from the probe body by a thin Rexolite® sleeve [17]. The dielectric portion of the probe that forms the secondary capacitance (C_E) is highlighted in yellow. In addition to its non-invasive nature the E-dot probe provides inherent noise immunity resulting from the attenuation of electromagnetic noise [18].

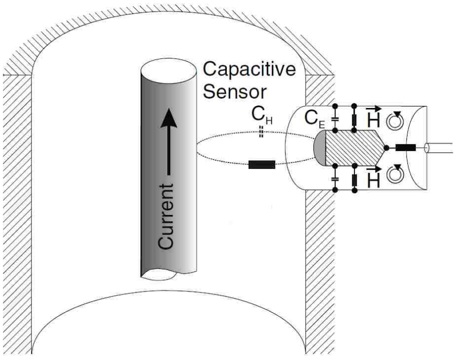

Figure 3.18: Example configuration of an E-Dot capacitive voltage sensor.

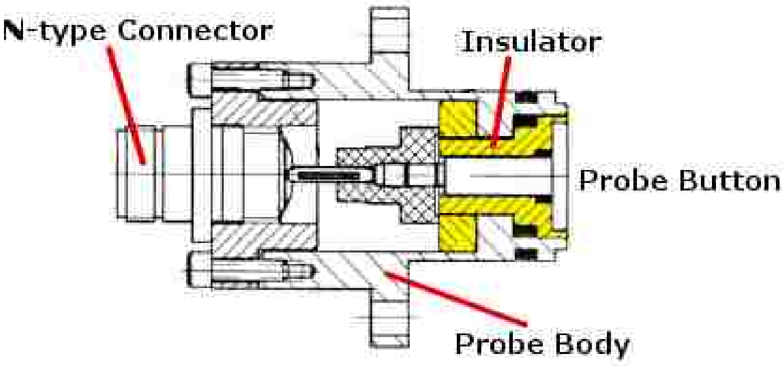

Figure 3.19: Schematic of the Axis-I E-dot probe.

Much like the previous section for the Rogowski coil, the E-dot probe was approximated by discrete circuit elements in SPICE as seen in Figure 3.20. From the final dimensions of the capacitor, the separation between the probe and the current carrying conductor is 2.185 inches, with an exposed probe area of 0.396 square inches. Neglecting fringe fields and using a simple parallel plate capacitor approximation for a water dielectric, the capacitance between the probe and conductor is approximately 3.25 pF. From [17], the capacitance between the probe and probe body (C_E) was calculated to be 5.3 pF. The resulting bandwidth of the E-dot with a 50 Ω termination was calculated to be 0.43 ns from

$$\mathrm{RC} = (\mathrm{R}_1 + \mathrm{R}_2) \cdot (\mathrm{C}_\mathrm{E} + \mathrm{C}_\mathrm{H}), \tag{3.13}$$

as was demonstrated in [17]. This is more than adequate to capture the anticipated

15 ns rise-time of the peaking capacitor. Using these values, a SPICE model was implemented as shown in Figure 3.20.

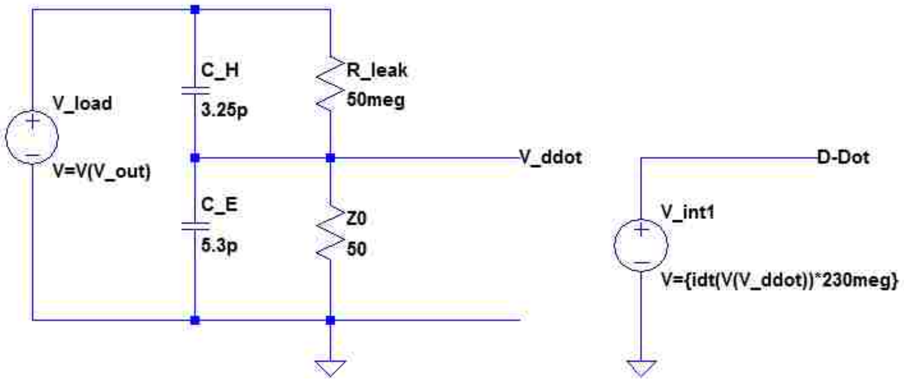

Figure 3.20: Discrete circuit element implementation of an E-dot in SPICE.

3.4 Mechanical Design and Field Modeling

Based on the optimal capacitance value determined in the previous sections the physical geometry of the peaking capacitor was chosen and electrostatic field models were created in ANSYS Maxwell [19] to determine whether breakdown issues would exist. In addition to the electrical characteristics of the capacitor, space constraints for the CTS had to be taken into account. The peaking capacitor was originally designed as an elongated 10-inch outer-diameter coaxial structure with a cable connection at each end, and an integrated spark-gap switch. This design was nearly 5 feet long, and had to be revised based on available space. To remedy this issue, a new design was selected, featuring a wider base that allowed for connection of both input and output cables at the top of the coaxial structure as seen in Figure 3.21. The overall height of the structure is still over 4 feet, but the top-fed design allows for a more suitable footprint as compared to the original design. The larger diameter also allowed for the easy addition of diagnostics and fittings to the top of the device.

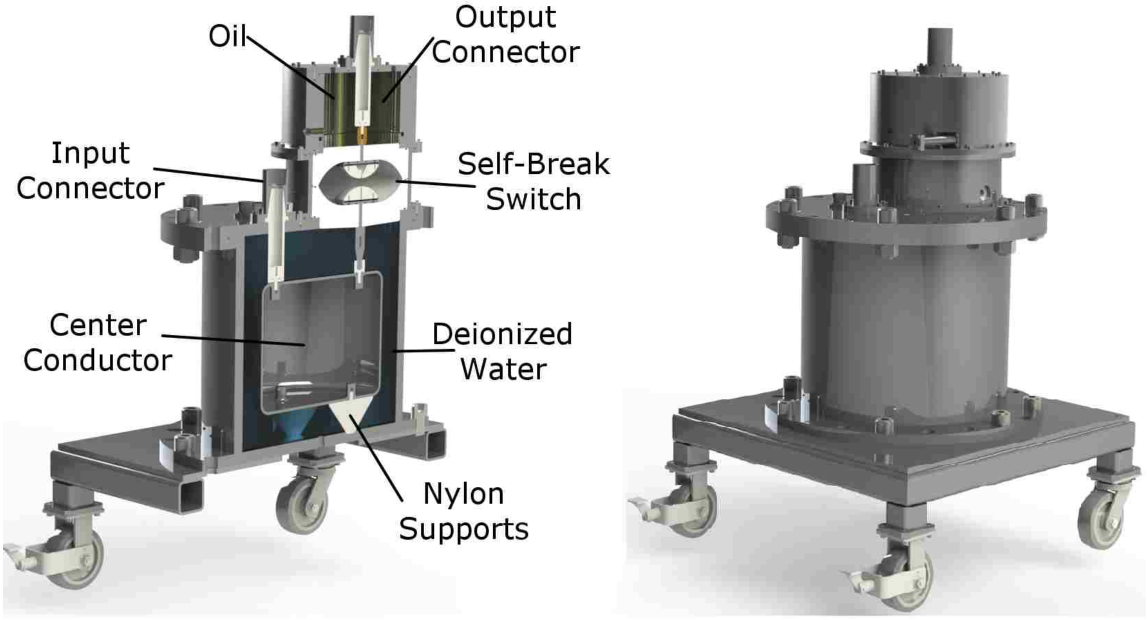

Figure 3.21: Rendering of the final peaking capacitor design.

3.4.1 Capacitor Geometry

As discussed in previous sections, a water-filled coaxial-capacitor geometry was chosen for its ease of construction, reliability, and availability of plumbing in the CTS enclosure. Additionally, in the event an electrical breakdown occurs inside the capacitor, water is not subject to catastrophic failure like solid dielectrics. To make the construction of the capacitor faster and cheaper, a Normal Pipe Size (NPS) 22 dimension pipe was used for the design. This pipe size was chosen because it has a 20 inch ID and 22 inch OD, similar to the dimension needed for a 12-inch-long section of coax capacitor at 7.8 nF using Eqs. (3.4), (3.5), and (3.7). It was later discovered that this specific size of pipe, although it falls within NPS standard, is somewhat esoteric and did not expedite procurement. A new set of parameters was established for the peaking capacitor as seen in Table 3.3 with a higher safety margin on the breakdown safety threshold. The use of a 22 NPS standard fixed the outer dimension of the capacitor, and the rest of the capacitor parameters were adjusted accordingly.

The optimal peaking capacitor dimensions occur when the electric field enhance-

Table 3.3: Final capacitor specifications from Section 3.2.

Capacitance (C)	Voltage (V_{MAX})	Pulse Width (τ_{eff})	Permittivity (ϵ_r)	OR (b)
7.8 nF	−350 kV	4 μs	80	10 in

ment inside the coaxial structure is equal to the peak breakdown field at the desired safety threshold. In this case, for a peak operating voltage of −300 kV the target voltage was set to −350 kV, adding a 50 kV safety threshold. The pulse length used to calculate maximum breakdown field was set to 4 μs, more than double the 1.8 μs pulse length of the PFN Marx unit in order to further increase the electric breakdown threshold. The first step in determining the peak field inside the capacitor was to rearrange Eq. (3.3) to create an expression for the inner radius based on the parameters from Table 3.3, given by

$$a = b \cdot \left[exp\left(\frac{2\pi\epsilon l}{C}\right)\right]^{-1}. \tag{3.14}$$

The length of the structure l, is swept over a range of values in order to find the point at which the peak and breakdown fields are equal. The results of Eq. (3.14) can then be inserted into (3.6), to determine the maximum field of the geometry. Next the area of the inner conductor can be approximated as a cylinder given by

$$\mathrm{A} = 4\pi\mathrm{a}^2 + 2\pi\mathrm{al}. \tag{3.15}$$

The maximum breakdown field can be determined for deionized water from J.C, Martin's breakdown formula show in Eq. (3.7), where k is a semi-empirically determined constant equal to 0.3 for deionized water [12]. The length of the structure at which Eqs. (3.6) and (3.7) become equal was then determined numerically using MATLAB, as shown graphically in Figure 3.22. The final dimensions from Figure 3.22 are shown in Table 3.4, and the MATLAB script used to generate these results is included in Appendix C.

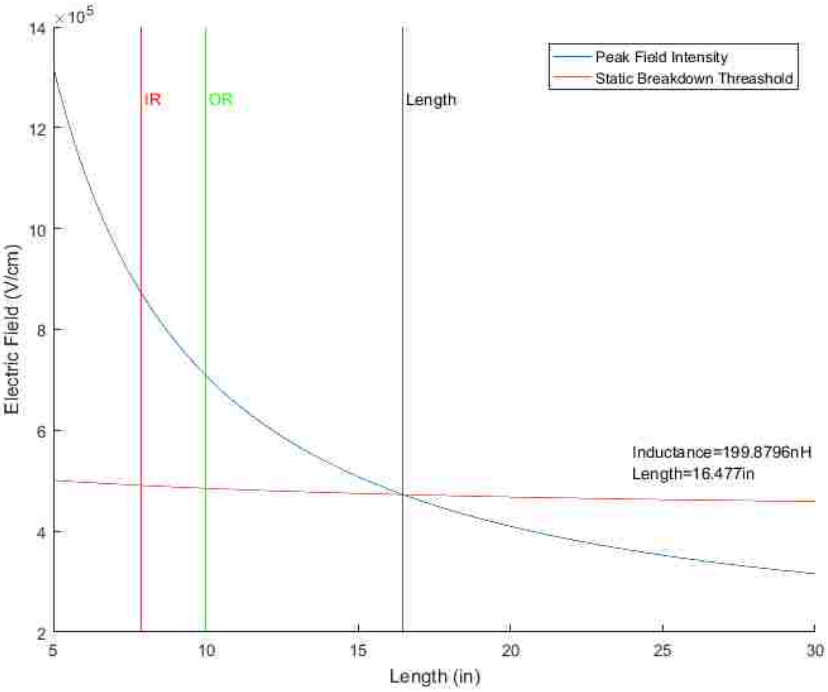

Figure 3.22: The capacitor dimensions with a fixed outer diameter.

Table 3.4: New capacitor parameters based on the fixed dimensions.

Length (inch)	OR (inch)	IR (inch)	Inductance (nH)	Peak Field (kV/cm)
16.477	10	7.815	199.88	472.7

In order to create a structure that was physically realizable, and maintain spacing within the capacitor structure, mechanical supports were inserted at the bottom of the central conductor, and cable ports were added to the top. The same style connector was used for the peaking capacitor as those employed on the PFN Marx unit. These connectors have the advantage of smooth integration with the existing hardware and cabling, sufficient voltage hold off, and proven reliability. The distance between the top lid of the peaking capacitor and the central conductor was then defined by lid thickness because these connectors are bolted to the exterior of the structure and have a fixed-length insulator that is inserted through a clearance hole. Using a readily available 1-inch-thick flange blank for the lid of the capacitor, this clearance was then set to 4.398 inches. The separation between the bottom of the cylinder and the base of the capacitor was set to 3 inches, lowering the peak field in this region well below the bulk breakdown strength of the water as shown in Table 3.4.

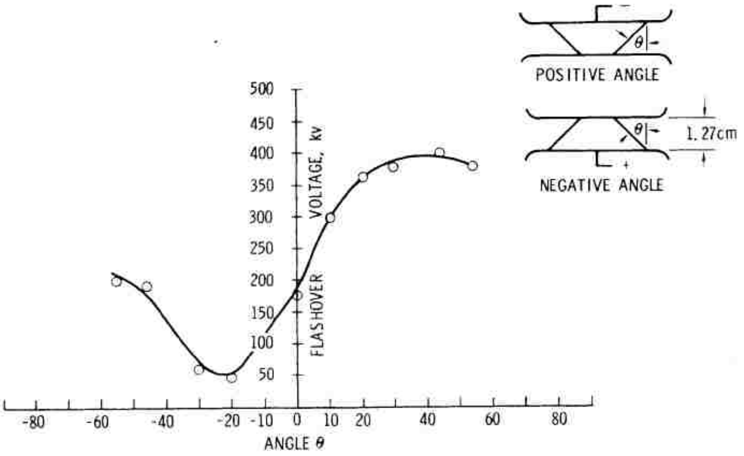

Figure 3.23: Flashover voltage versus θ for Lucite [20].

Next the supports on the bottom of the conductor were chosen to be cast nylon frustums with a 40° angle. Due to the high surface flashover strength of cast nylon and compatibility with deionized water, it is one of the best available materials for this application [20]. The angle of the frustum was chosen for optimal surface flashover hold-off in accordance with the work done by Osborne Milton [20], as seen in Figure 3.23 for Lucite. A cross section of the support structure design can be seen in Figure 3.24.

3.4.2 Finite Element Analysis

Using the results of the previous section, a finite element analysis (FEA) model was created. This analysis is necessary because the analytical results from the previous section are based on approximations for a perfectly cylindrical geometry that ignores fringe fields and field enhancements along its edges. In the final construction of the capacitor, 1-inch-radius fillets were added to the central conductor of the peaking capacitor in order to reduce field enhancements. These fillets further distort the geometry as compared to the perfectly cylindrical approximations used in the previ-

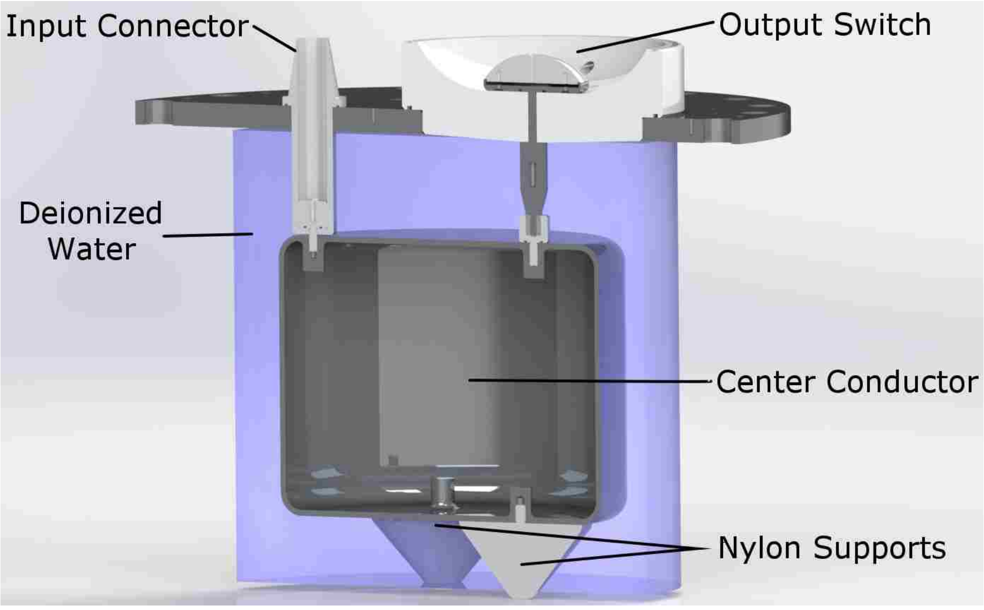

Figure 3.24: Cut away of the peaking capacitor showing the nylon support structure.

ous section, and alter the capacitance of the structure. For the parameters listed in Table 3.4, an FEA model was created in ANSYS Maxwell for an excitation voltage of −350 kV. The length of the inner conductor, between the top and bottom surfaces, was set to 16.5 inches as opposed to the calculated estimate of 16.477 inches. The resulting fields are shown in Figure 3.25, and the resulting capacitance of the simulated structure was 10.118 nF. Figure 3.25 shows a two dimensional cross section of the simulated electric field results for a full three dimensional structure. The highest fields exist within the dielectric of the input connector, but this connector has demonstrated reliability at this operating voltage and pulse length in existing applications.

As expected the simulated capacitance results were much higher than the analytical approximations. In order to reduce the capacitance to the desired value of 7.8 nF, the length of the structure had to be reduced. To correct these dimensions, Eq. (3.3) was used to determine the appropriate change in length needed to reduce the capacitance by ~ 2.3 nF. The section of coaxial capacitor with the same dimensions needed to achieve 2.3 nF is 5.02-inches-long. The length was then reduced to 11.5 inches and after minor adjustments, a final length of 11.75 inches was selected to produce a capacitance close to 7.8 nF (7.9035 nF actual). The resulting field model

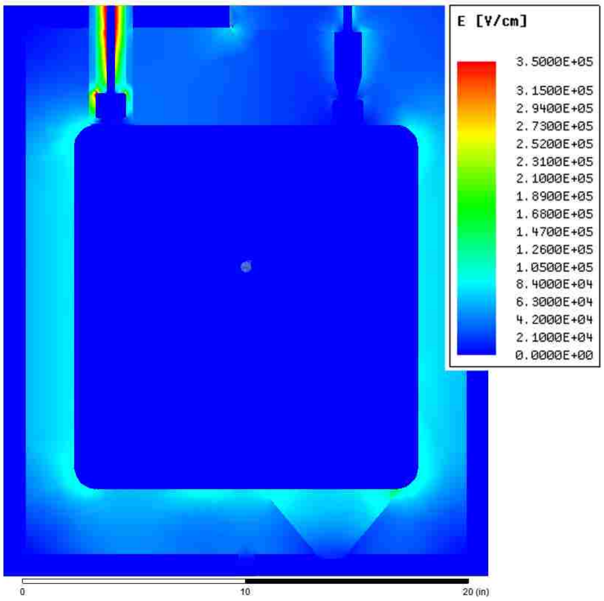

Figure 3.25: ANSYS electric field model for a capacitor with the specifications in table 3.4.

is shown in Figure 3.26.

The electric field inside the water section of the peaking capacitor had a peak value of $\sim 100\,\mathrm{kV/cm}$ along the coaxial section, and a maximum field of $\sim 190\,\mathrm{kV/cm}$

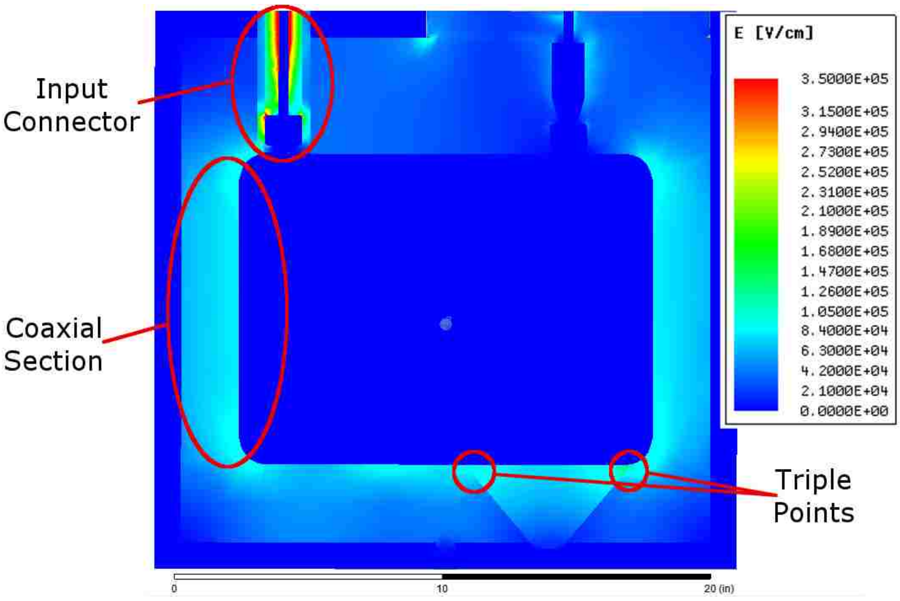

Figure 3.26: Electrostatic field model with the capacitor dimensions modified to achieve 7.8 nF.

at the triple point between the nylon feet, water, and center conductor seen in Figure 3.26. These values fall well below both the peak field calculated in Table 3.4, and the surface flashover field of $> 300\,\mathrm{kV/cm}$ determined by Milton [20].

3.5 Spark Gap Design

To achieve rise-time sharpening, controlling the peaking switch breakdown voltage is critical. If the switch closes too early during the voltage rise, the rise-time will not be shortened enough and the pulse will be degraded. If it closes too late, the voltage will begin to double via resonant charging; because the circuit is a CLC (Capacitor-Inductor-Capacitor) network with a large initial capacitance ($\mathrm{C_{PFN}} = 70\,\mathrm{nF}$) and a relatively small final capacitance ($\mathrm{C_{peak}} = 7.9\,\mathrm{nF}$) [21]. If the switch does not breakdown, the voltage across the peaking capacitor will rise according to [21]

$$\mathrm{V_{MAX}} = \frac{2\mathrm{V_0}}{1 + (\mathrm{C_{peak}}/\mathrm{C_{PFN}})}. \tag{3.16}$$

For the given capacitance estimates, the resulting peak voltage is 1.8X the input voltage.

A pair of copper-tungsten alloy electrodes of the type used in the DARHT Axis-I laser-triggered Blumlein switches were employed for the self-breakdown switch. Although these electrodes have a graded radius, the portion of the electrode surface where breakdown is likely to occur has a radius of 3.276 inches, which was used for the initial gap-spacing calculations. The field enhancement between two spherical electrodes with an applied voltage $\mathrm{V_0}$, radius r, and separation a can be determined using [14]

$$E_{max} = 0.9\frac{V_0}{a} \cdot \frac{r + a/2}{r}. \tag{3.17}$$

Choosing an initial gap separation of 0.7 inches, the field between the electrodes will be roughly equal to $0.56\mathrm{V_0}\,(\mathrm{V/cm})$.

Next, the electric field intensity required for a self-breakdown gap under pulsed conditions can be calculated using [12]

$$\mathrm{E}^{\pm}_{\mathrm{bdm}} \cdot \tau_{\mathrm{eff}}^{1/6} \cdot \mathrm{d}^{1/6} = \mathrm{k}^{\pm} \cdot \left[\mathrm{P}/\mathrm{P}_0\right]^{\mathrm{n}}. \tag{3.18}$$

This equation takes into account the gap separation d in centimeters, the pressure between the electrodes P in PSI, and the pulse length τ_{eff} in microseconds. The constants $k^{\pm}$ and n are empirically determined for each gas under positive and negative polarity, and P_0 is atmospheric pressure. The resulting breakdown field $\mathrm{E}^{\pm}_{\mathrm{bdm}}$ is given in megavolts per centimeter [22]. For the peaking capacitor using an SF_6 filled negative polarity gap, $k^{\pm}$, n, d, and τ_{eff} are equal to, 74, 0.4, 1.78 cm, and $\sim 100\,\mathrm{ns}$ respectively. The resulting output of breakdown electric field versus gap pressure is shown in Figure 3.27. Because these values were experimentally determined by J.C. Martin using a $50\,\mathrm{kV}/\mu\mathrm{s}$ ramped voltage pulse (as compared to $\sim 1.5\,\mathrm{kV/ns}$ for this case), the resulting breakdown field will only provide a rough approximation and, once constructed, the peaking switch had to be characterized and eventually modified.

In order to use the DARHT Axis-I Blumlein-switch electrodes, mounting brackets were fabricated as seen in Figure 3.28. The switch insulator material was chosen to be

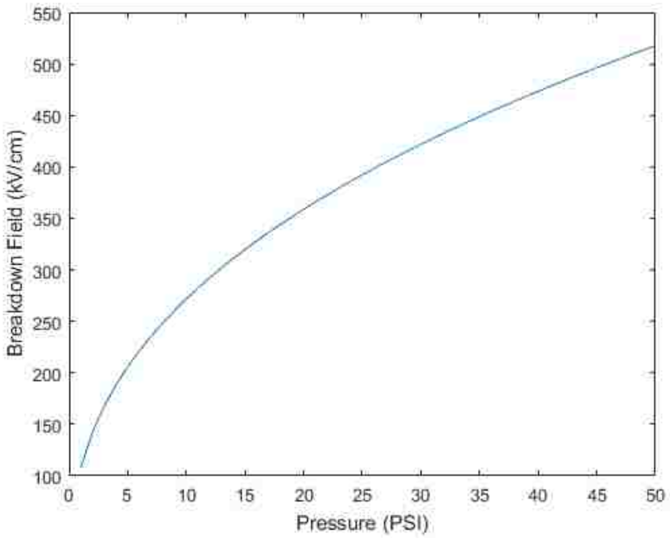

Figure 3.27: Pulse charged self-breakdown electric field curve for SF_6 [22].

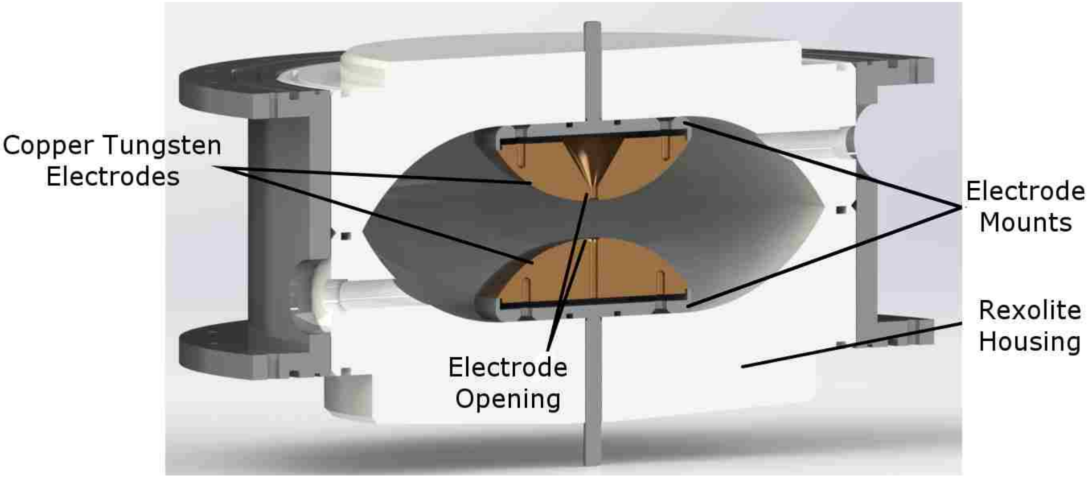

Figure 3.28: Rendered cross-section of the final switch design.

Rexolite® because of its structural rigidity, high dielectric strength ($270-470\,\mathrm{kV/cm}$ [23]), and surface flashover resistance ($> 197\,\mathrm{kV/cm}$ @ 45° [20]). This design proved to be adequate up to the required fields along the Rexolite® surface, but due to an oversight by the author, the gas ports were added as an afterthought and an analysis of the electric fields in this region was not performed. This led to surface flashover and subsequent punch-through of nylon pressure fittings during testing at -150 kV. This issue will be further discussed in Section 5.

Since the electrodes used for this application were originally designed for a laser triggering scheme, there is a clearance hole through their axis and a small radius

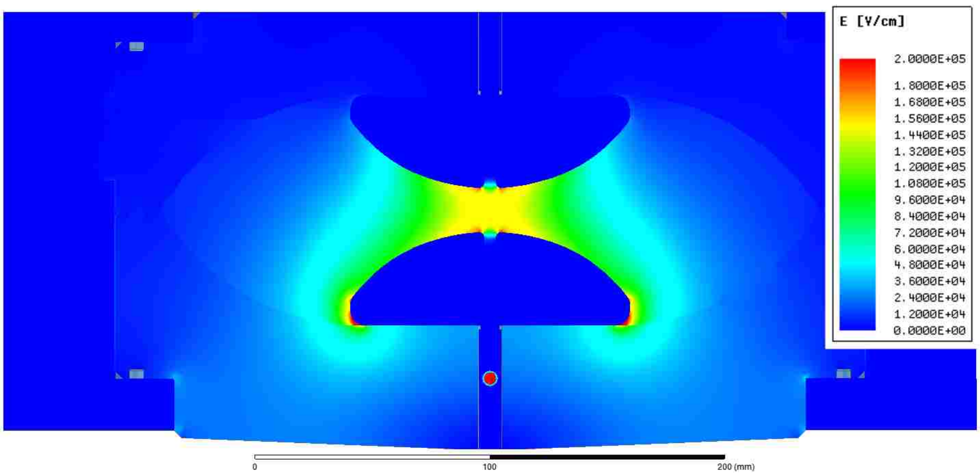

Figure 3.29: Electric field model of the spark gap switch at -300 kV charge prior to closure.

around this opening at the center of the electrode as seen from the switch cross section in Figure 3.28. This feature creates a larger field enhancement than was calculated for the simple sphere-sphere geometry from (3.17) alone. In order to determine the resulting fields, a three dimensional model was created in ANSYS Maxwell. As seen in Figure 3.29, the average field between the electrodes is roughly 150 kV/cm for a −300 kV applied voltage, which is consistent with the peak field of 168 kV/cm determined in Eq. (3.17). However, due to the field enhancements caused by the clearance holes, the peak field is increased to 200 kV/cm at the electrode surface. Applying this value to Figure 3.27, the approximate peak pressure of SF_6 needed to operate the switch up to −300 kV will fall just below 10 PSIG. In order to ensure safety in operation, and allow for flexibility (including the use of dry air), the switch housing was designed and certified to operate up to 100 PSIG. As will be seen in Section 4, this design became problematic because precise control of SF_6 pressure below 10 PSIG was not possible with the available regulation and recapture system.

In this chapter, the design process for the peaking circuit was detailed, and the final design presented. In addition, full scale circuit models were developed for the Axis-II PFN Marx generator that were used to verify the peaking circuit design. A 7.8-nF water filled capacitor with a self-break pressurized spark gap switch was designed, modeled, and constructed. Once assembled, the peaking capacitor was tested with the PFN Marx unit and the results are presented in Chapter 4.

Chapter 4

Results

Prior to the addition of the peaking capacitor, baseline data was taken using only the PFN and a $130-\Omega$ dummy load. This testing allowed for the accurate characterization of the circuit's rise-time for a range of operating voltages prior to the addition of the peaking capacitor. As seen in Figure 4.1, the voltage measured for a $-30\,\mathrm{kV}$ PFN charge from both the resistive divider (CVM Voltage) and the load E-dot (E-Dot Voltage) are shown for the full pulse (a), and the rising edge with the 10 % and 90 % amplitudes annotated (b). The rise-time for a $-30\,\mathrm{kV}$ charge, as averaged over 7 samples, was 90 ns measured from the CVM. Repeating this method for charge voltages from -40 to $-80\,\mathrm{kV}$, the rise-times varied from 85 to 89 ns. The E-Dot and CVM sensors are integrated into the load chassis and the signals were measured through a $\sim$ 60-foot-long section of $50-\Omega$ coaxial cable. The rise-times measured from the integrated load E-dot varied between 95 and 101 ns with an average of 98 ns. There exists an error of ±2 ns in the rise-time measurements due to the 1 ns resolution of the measured data at the 10 % and 90 % amplitude crossings. In addition, the distribution of this error may be skewed due to measurement bias by the author as the amplitude crossings were rounded up to the nearest nanosecond. The PFN jitter, measured from the load resistor E-dot for the same 7 samples at $-30\,\mathrm{kV}$ charge, varied over a range of 10 ns with a standard deviation of 7.5 ns. The switch jitter was measured using the negative slope of the rising pulse edge as it crossed the −50 kV threshold.

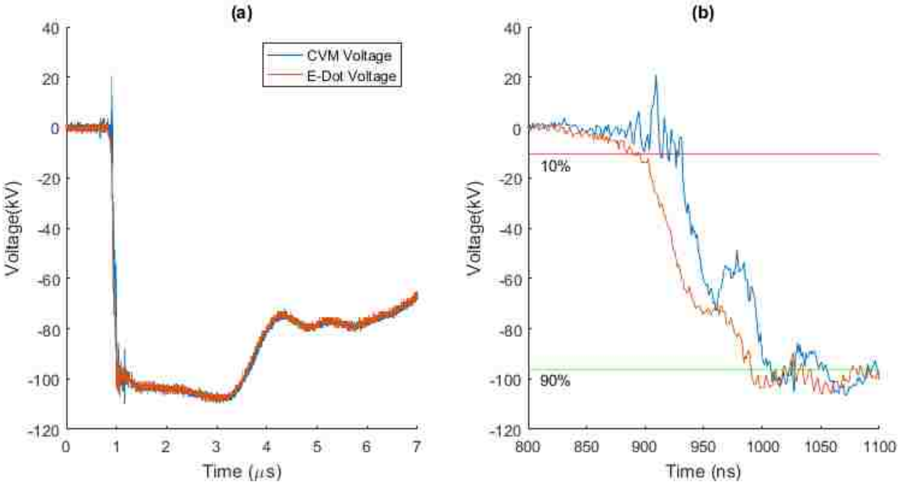

Figure 4.1: PFN output into a 130 Ω load at −30 kV charge.

The peaking capacitor was installed in the CTS enclosure and connected to the PFN unit through a 25-foot-long section of Dielectric Sciences 2077 cable [24] as seen in Figure 4.2. The output of the self-breakdown switch was connected through another 8-foot-long section of 2077 cable to the load. In order to determine the correct operating pressure for the switch at each charge voltage, it was tested for a sweep of pressures. Testing was done with a −30 kV PFN charge (−100 kV load voltage); however, when the charge voltage was increased to −40 kV (−130 kV output voltage) a breakdown occurred along one of the pressure feedthroughs that shorted the pulse and testing had to be halted. The data obtained for −30 kV charge was taken over a range of pressures from 3 − 18 PSIG. The measured rise-times ranged from 14 to 19 ns which falls roughly within the ±2 ns measurement error. Figure 4.3(a) shows both the load and capacitor voltages during the pulse, and Figure 4.3(b) shows a more detailed view of the rising edge with the 10 % and 90 % amplitudes marked.

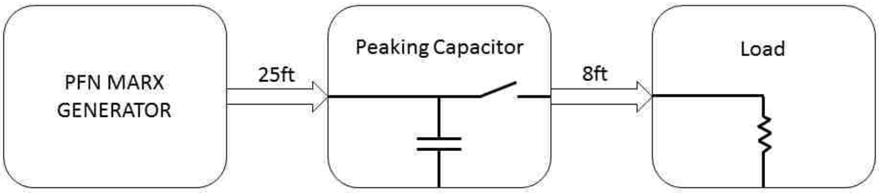

Figure 4.2: Connection block diagram of the peaking circuit during testing.

The waveform shown in Figure 4.3 was taken with a switch pressure of 9 PSIG, and the rise-time is 18 ns. The voltages were measured from the E-Dot built into the peaking capacitor lid and the E-Dot integrated into the load resistor chassis. As can clearly be seen in Figure 4.3 (a), the peaking capacitor is pulse charged by the PFN up to a peak voltage, at which point the switch closes and a sharpened rise-time pulse is delivered to the load.

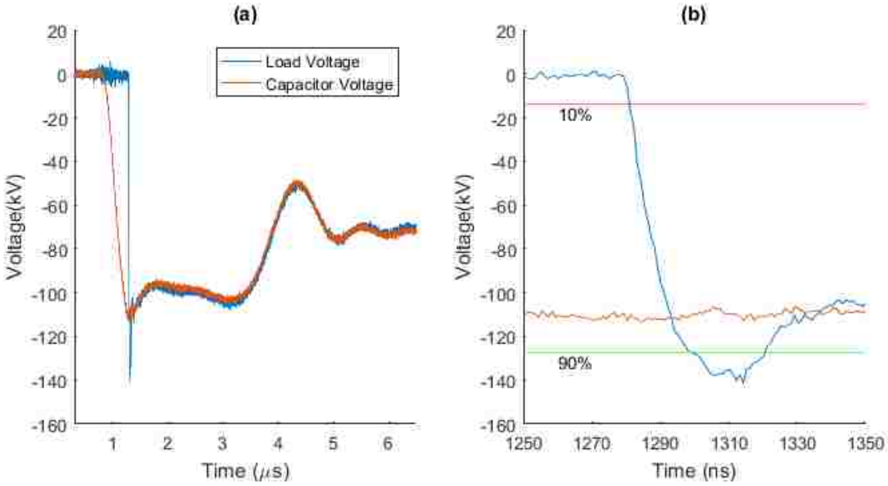

Figure 4.3: Measured peaking capacitor and load voltage waveforms shown for a full timescale (a) and the peaked output rising edge (b).

Five shots were taken for pressure settings from $3 - 16$ PSIG of dry air in 1 PSI steps, and the switch closure times were measured for each. The range and standard deviation of closure times were calculated at each pressure and these results are plotted in Figure 4.4. From Figure 4.4, there does not appear to be any clear trend in switch jitter for the pressures used, and above 16 PSIG the switch would not close reliably for the given charge voltage. This variation may in part be due to the small sample size used for each jitter measurement. Regardless of the statistical validity of these measurements, it is clear that for use with a velvet cathode, this range of switch closure times makes this peaking capacitor unreliable. With a total PFN pulse length of about 2 μs , a peak jitter of a microsecond in switch closure time creates a 50 % variation in the output pulse length. Potential resolutions for this issue will be discussed in Chapter 5.

A voltage spike can be observed at the beginning of the sharpened output pulse

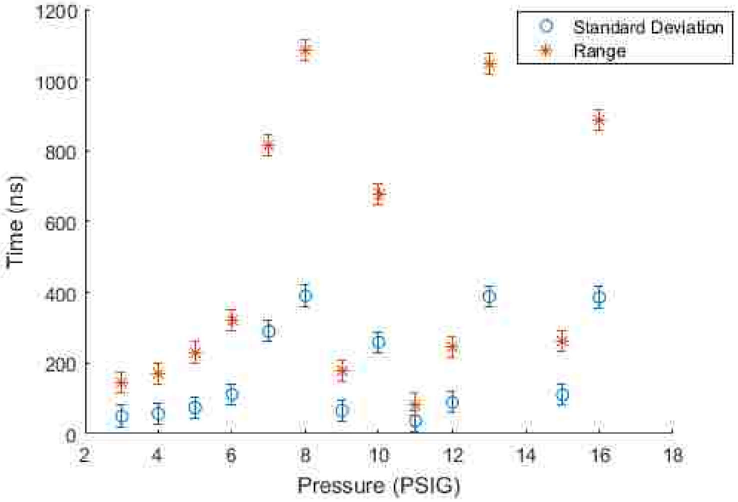

Figure 4.4: Jitter measurements for range of pressures for a −30 kV PFN Marx generator charge.

seen in Figure 4.3. In order to verify that this spike is the result of resonant charging as discussed in Section 3.5, the peak amplitude of voltage overshoot was measured for each shot. This data was plotted against the switch closure delay for all pressures as seen in Figure 4.5. A clear trend of increasing amplitude emerges that levels off at roughly 150 kV. Assuming that V_0 from (3.16) is equal to −100 kV for a −30 kV PFN charge, and that the peak voltage V_{MAX} is −150 kV, then the effective PFN capacitance is 23.4 nF. The output inductance of the circuit can also be determined from the rise-time assuming the peaking capacitance is 7.9 nF. When the switch is closed the peaking capacitor, output cable, and load form an RLC circuit, and the natural frequency of this circuit can be estimated using

$$\omega_0 = \sqrt{\frac{1}{LC}}. \tag{4.1}$$

The natural frequency can be approximated as 17 MHz based on the quarter cycle rise-time of the peaking capacitor. The output inductance is calculated to be 461.54 nH by rearranging (4.1). This seems to be a reasonable approximation based on the series inductance of the peaking capacitor calculated in Table 3.4, combined with the inductance of the 8-foot-section of 2077 cable and load resistor.

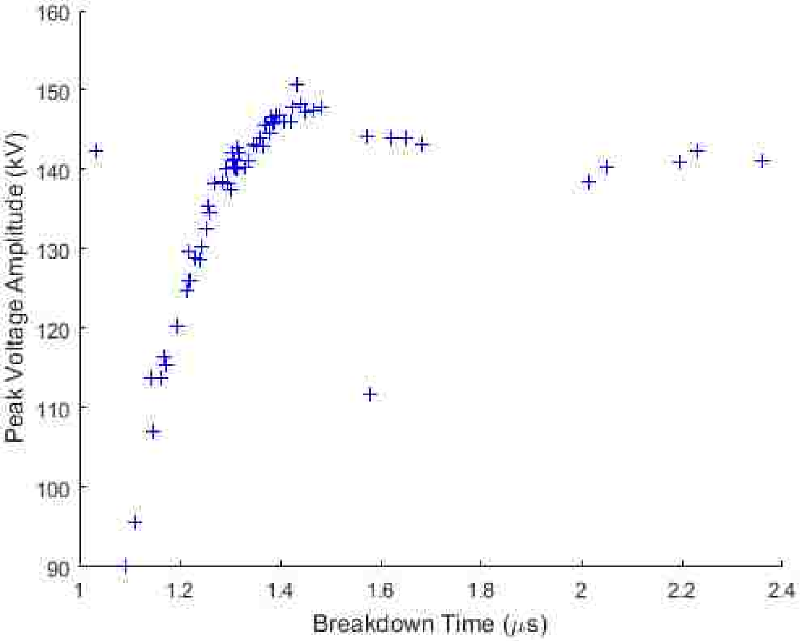

Figure 4.5: Peak output amplitude versus breakdown delay on the peaking switch.

In this chapter, experimental test results were presented for the peaking circuit described in Chapter 3. Through the testing process, a number of issues were discovered that will be addressed in greater detail in Chapter 5. The problems of primary concern are the large switch closure jitter and surface flashover along the Rexolite® switch housing. Potential solutions to these issues are proposed, and conclusions are presented.

Chapter 5

Future Work and Conclusions

During the testing of the peaking capacitor, two issues of primary concern were discovered: 1) surface flashover between the switch electrode and the grounded outer structure; and 2) the large jitter in switch closure times. The first issue limited the operating voltage to less than half of the target −300 kV operation. Upon inspection of the breakdown path, it was immediately apparent that this area was overlooked by the author, and electric field models had not been developed to investigate the breakdown risk in the highlighted area of Figure 5.1. In order to resolve this issue and ensure that breakdown would not occur during normal operation of the switch, field models were developed in order to determine the fields that existed at breakdown shown in Figure 5.2.

Surface flashover occurred during four shots at a PFN charge voltage of $-40\,kV$ which translated to a voltage of approximately −150 kV at the load. Since the flashover took place late in time during all breakdown events, the field models were conducted for the switch configuration after closure (both electrodes at −150 kV). From Figure 5.2 the peak field at breakdown was roughly 100 kV/cm near the edge of the electrode. In addition to high field enhancements from the electrode geometry in this region, a triple point exists between the electrode mount, the Rexolite® insulator, and the pressurized air. In order to mitigate fields in this region and increase surface distance to ground, changes to both the electrode and grounded

Figure 5.1: Surface breakdown path shown along the Rexolite® insulator in red.

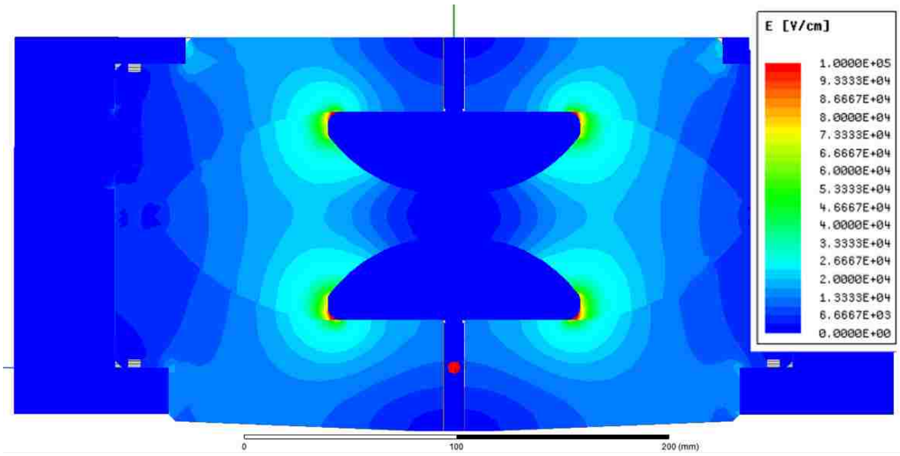

Figure 5.2: ANSYS model of the electric fields inside the closed switch at 150 kV voltage.

support structure were tested in ANSYS Maxwell. The field models employed for the new switch configuration use a −300 kV electrode voltage in order to ensure that the fields are representative of the maximum operating voltage. The first revision shown in Figure 5.3 has a wider clearance on the outer switch housing with 1/4 inch fillets added to the edges (whereas the previous version had no fillet). This configuration both increased the breakdown distance by increasing the clearance radius from 0.75 inches to 1.6 inches, and reduces the field enhancements along the sharp edge of the clearance hole. A comparison between resulting fields of the current configuration and the modified housing configuration at −300 kV electrode voltage can be seen in Figure 5.4.

Figure 5.3: Rendering of the switch housing with a modified clearance around the pressure fitting.

The next modification to address the switch breakdown issue was the modification of the switch electrodes. The electrodes used in the peaking capacitor switch were chosen because of availability and are not ideally suited for this configuration. By reducing the overall diameter of the electrodes, the surface flashover distance can be greatly increased and field enhancements at the triple point can be reduced. To this end, a new set of electrode dimensions were chosen that have a reduced diameter and larger fillet radius at the bottom of the electrode. The new radius of the electrodes was chosen to be 1.6 inches and the new edge fillet, where the electrode meets the Rexolite, was chosen to be 0.5 inches. The resulting fields for −300 kV electrode voltage are shown in Figure 5.5 and Figure 5.6 for 300 kV/cm and 27 kV/cm field scaling, respectively. These two different field scalings allow for the detailed examination of the electric fields in both the electrode region and the pressure access port regions. For a −150 kV excitation these changes reduced the simulated peak field at the triple points from 27 kV/cm with the original electrodes to 13 kV/cm for the new electrode design.

In order to address the large switch jitter for self-breakdown switches, there are two primary parameters that contribute, switch pressure and gap spacing [22]. The

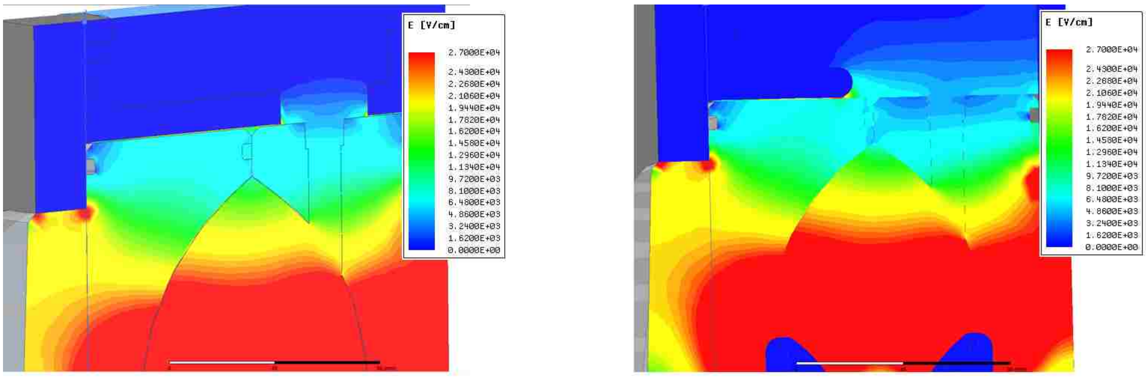

(a) **(b)**

Figure 5.4: Comparison of electric field intensities between the current configuration (a) and the modified housing configuration (b).

higher the switch pressure and the narrower the gap, the lower the jitter will be. The improved jitter performance is due to the fact that in order to attain switch closure, sufficient energy must be available to accelerate charge carriers across the gap to establish and sustain ionization and therefore conduction. Because the charge carriers will have an initial velocity distribution, some of them will cross the gap sooner than others making the switch closure time a statistical event based on the initial condition of these carriers [22]. To this end, in future revisions of the switch design the gap spacing will be reduced such that the maximum 100 PSIG pressure of the switch can be utilized. In addition, a sharper radius on the switch electrode can be utilize to increase field enhancement in the gap and further reduce the jitter by reducing this statistical nature of the charge carriers. If these modifications do not reduce the 1-σ jitter of the self-breakdown switch to less than 40 ns, a triggered field effect switch topology may need to be employed.

Once these issues are overcome, a crowbar unit will be added to the circuit between the PFN Marx and the peaking capacitor in order to control the length of the pulse delivered to the load. Since the switching jitter of the peaking capacitor will be compounded with the jitter of both the PFN Marx and crowbar units, it is of vital importance that it be reduced as much as possible. Since one of the primary parameters of interest for the CTS is the variation of applied pulse length, the overall quality of data may hinge on the jitter parameters achievable between the peaking

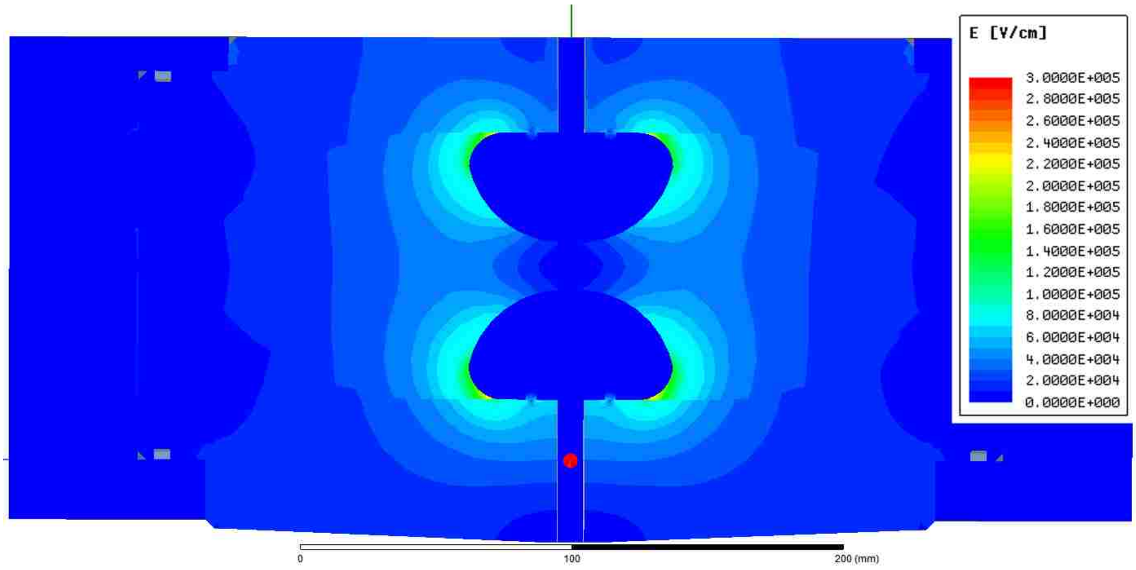

Figure 5.5: Modified electrode electric field intensity with a −300 kV charge and 300 kV/cm field scale.

capacitor and crowbar unit.

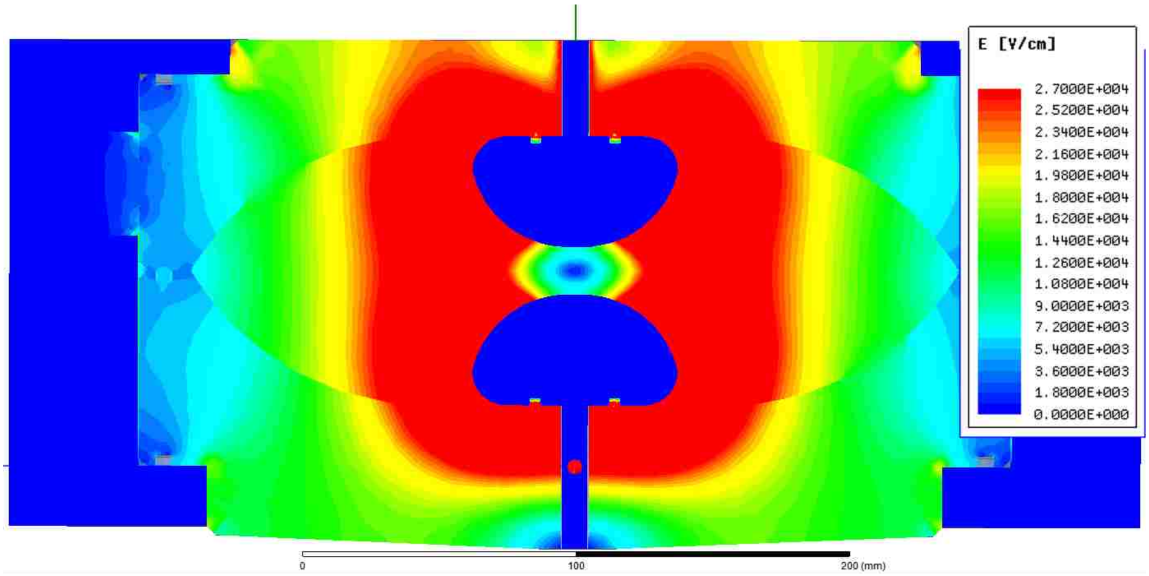

Figure 5.6: Modified electrode electric field intensity with a −300 kV charge and 27 kV/cm field scale.

5.1 Conclusions

A pulse sharpening circuit was designed, constructed, and tested at LANL for use with an explosive emission cathode. The 10 − 90% rise-times from an existing PFN Marx unit were reduced from nearly 100 ns to about 15 ns with the addition of a peaking capacitor circuit. The results of experimental testing of the PFN Marx unit agree well with simulated results in SPICE both with and without the addition of the peaking capacitor circuit. However, there are still issues that need to be resolved before this circuit becomes useful for cathode testing. These issues include the resolution of surface tracking within the peaking capacitor self-breakdown switch, and the reduction of switch jitter. Once these issues are resolved, the peaking capacitor will be integrated into a velvet cathode test stand to evaluate the performance of different cathode geometries under varying pulse lengths.

Appendix A

Self break spark gap sub-circuit used to model the peaking switch.

```
.subckt spark_gap 1 4
R_off 1 2 1e11 ; dark resistance (affects breakdown voltage)
R_ion 1 2 R=10/V(ion)**.75 ; dynamic ionization resistance
Dfall 2 3 10V ; bidirectional cathode fall voltage
V_ion 3 4 0 ; current sense for behavioral sources
B_ion 0 ion I=I(V_ion)**2 ; measure of channel ionization
C_ion ion 0 190n Rpar=1 ; ionization time constant
.model 10V d(Vfwd=10 Vrev=10 Ron=10m)
.ends spark_gap
```

Appendix B

Full LTspice model of the Type-E PFN Marx circuit.

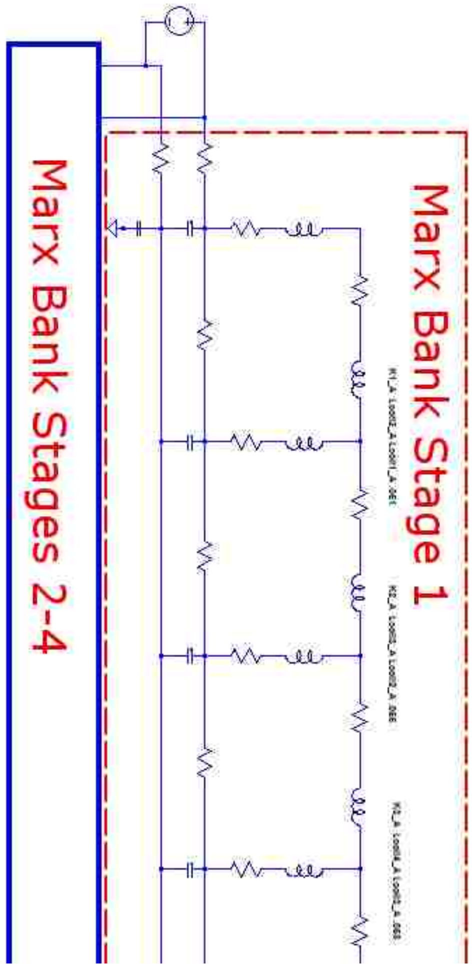

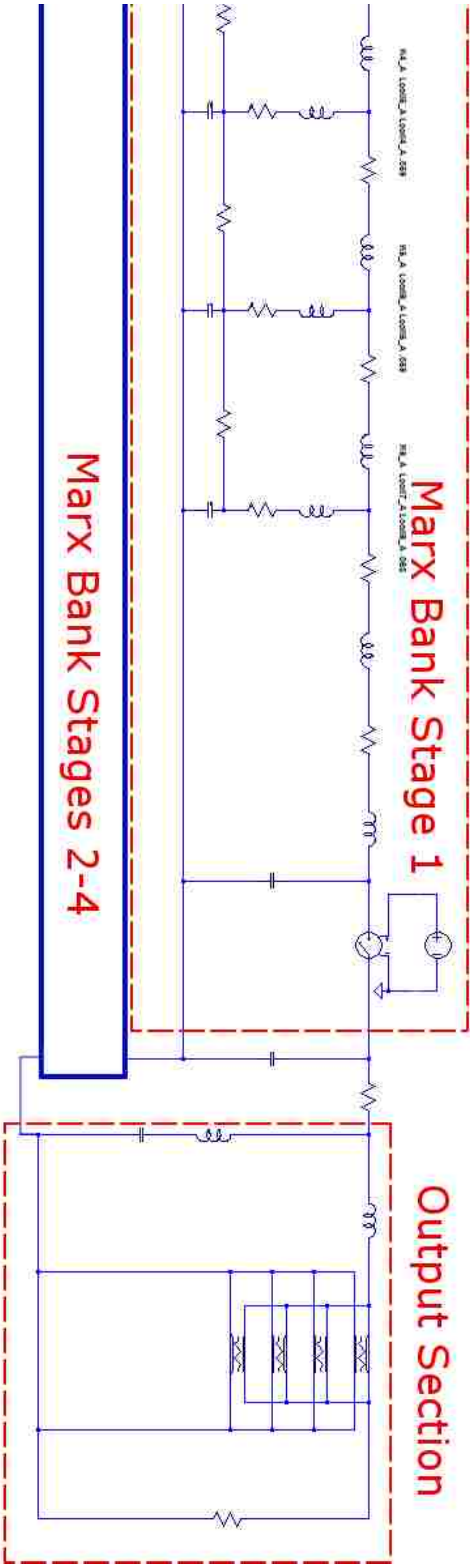
Marx Bank Stage 1
Marx Bank Stages 2-4
Output Section

Appendix C

MATLAB script used to determine dimensions of a coaxial capacitor.

```
%% Capacitor Dimensional Calculations Fixed OR

% House Keeping
clear all
close all

% Define Constant Parameters
C = 7.8e-9;          % Desired Capacitance
V = 350e3;           % Desired operational voltage
tau = 4;             % Pulse width at 65% peak voltage in us

epso = 8.854e-12;    % Permittivity of free space
epsr = 80;           % Relative Permittivity
eps = epsr*epso;     % Permittivity

muo = 4 *pi * 10e-7;% Permeability of free space
mur = 1;             % Relative Permeability
```

```
mu = muo*mur;       % Permeability



% Define Length

Li = 5:.001:30;         % Length in Inches 16.4772 target

Lm = (Li.*.0254);       % convert inches to meters


% Define OR

bi = 10;        % Outer capacitor radius in inches

bm = bi*.0254;  % OR in meters


% Calculate inner radius based on fixed capacitance

lnba = (2* pi * eps * Lm)/C;    % ln(b/a) i.e. ln(od/id)

ba = exp(lnba);                 % Ratio of od/id

am = bm./ba;                    % Inner radius in meters

ai = am/.0254;                  % IR in inches


% Seperation between inner and outer conductors

d = (bi-ai);


% Series Inductance

ind = (mu/(2*pi)).* lnba .* Lm;


% Field Enhancements from Ness Engineering

Efef = V./(ai.*log(bm./am));


% Breakdown voltage from J.C. Martin

% valid for 10us > tau > .1us

% A is in cm^2

% tau is in us

k = .3;    % For Water k+ = 0.3  k- = 0.6
```

```
A = 2 * pi .* (am.*100).^2 + 4*pi.*(am*100).*(Lm*100); % Area in cm^2

% Emax elictric field above static breakdown voltage in MV/cm
Emax = k./((tau^(1/3)) * (A.^(1/10)));
Emaxi = (Emax * 2.54 * 1e6);                % Emax in volts per inch

% Minimum Radius and length
[Y, I] =  min(abs(Emaxi - Efef));
amin = ai(I);
bmin = amin + d(I);
Lmin = Li(I);

% E-dot Sensor Area and Ch
A = .0254*pi*(.5/2)^2; % 1/2 inch diameter E-dot area

Ch = (eps*A)/(.0254*bmin*log(bmin/amin));

figure()
hold on
H = plot(Li, Efef.*2.54);
ylabel('Electric Field (V/cm)')
xlabel('Length (in)')
plot(Li, Emaxi.*2.54)
legend('Peak Field Intensity', 'Static Breakdown Threshold')



Xl = H.Parent.XLim;
Yl = H.Parent.YLim;

 line([amin amin], Yl, 'color', 'r')
 text(amin+.1, Yl(2)*(.9), 'IR', 'Color', 'r')
```

```
 line([bmin bmin], Yl, 'Color', 'g')
 text(bmin+.1, Yl(2)*(.9), 'OR', 'Color', 'g')

 line([Lmin Lmin], Yl, 'Color', 'k')
 text(Lmin+.1, Yl(2)*(.9), 'Length', 'Color', 'k')

 Xshift = .8;

 text(Xl(2)*Xshift, Yl(2)*.4, strcat('Inductance=', ...
...num2str(ind(I)*1e9),'nH') , 'Color', 'k')
 text(Xl(2)*Xshift, Yl(2)*.37, strcat('Length=', ...
...num2str(Li(I)),'in') , 'Color', 'k')
```

References

[1] R. B. K. Takayama, *Induction Accelerators.* Verlag Berlin Heidelberg, Germany: Springer, 2011.

[2] R. B. Miller, “Mechanism of explosive electron emission for dielectric fiber (velvet) cathodes,” *Journal of Applied Physics*, vol. 84, no. 7, pp. 3880–3889, 1998.

[3] J. Benford, J. Swege, and E. Schamiloglu, “High power microwaves, 3rd edition,” 2015.

[4] C. Ekdahl, “Modern electron accelerators for radiography,” in *PPPS-2001 Pulsed Power Plasma Science 2001. 28th IEEE International Conference on Plasma Science and 13th IEEE International Pulsed Power Conference. Digest of Papers (Cat. No.01CH37251)*, vol. 1, pp. 29–34 vol.1, June 2001.

[5] J. E. Coleman, D. R. Welch, and C. L. Miller, “Scattered hard x-ray and γ-ray generation from a chromatic electron beam,” *Journal of Applied Physics*, vol. 118, no. 18, p. 184505, 2015.

[6] J. E. Coleman, D. C. Moir, M. T. Crawford, D. R. Welch, and D. T. Offermann, “Temporal response of a surface flashover on a velvet cathode in a relativistic diode,” *Physics of Plasmas*, vol. 22, no. 3, p. 033508, 2015.

[7] D. Shiffler, M. Haworth, K. Cartwright, R. Umstattd, M. Ruebush, S. Heidger, M. LaCour, K. Golby, D. Sullivan, P. Duselis, and J. Luginsland, “Review of cold cathode research at the air force research laboratory,” *IEEE Transactions on Plasma Science*, vol. 36, pp. 718–728, June 2008.

[8] X. Lian-Sheng, Y. An-Min, C. Yi, Z. Huang, L. Xing-Guang, L. Jin, J. Xiao-Guo, Z. Kai-Zhi, S. Jin-Shui, D. Jian-Jun, and Z. Lin-Wen, “Multi-pulsed intense electron beam emission from velvet, carbon fibers, carbon nano-tubes and dispenser cathodes,” *Chinese Physics C*, vol. 34, no. 11, p. 1733, 2010.

[9] K. E. Nielsen, M. A. Bastian, W. L. Gregory, M. Sanchez, and C. R. Rose, “Maintaining high reliability PFN Marxes on DARHT II,” in *2015 IEEE Pulsed Power Conference (PPC)*, pp. 1–6, May 2015.

[10] B. Prichard, J. Barraza, M. Kang, K. Nielsen, F. Bieniosek, K. Chow, W. Fawley, E. Henestroza, L. Reginato, W. Waldron, R. Briggs, T. Hughes, and T. Genoni, "Technological improvements in the darht ii accelerator cells," in *Proceedings of the 2005 Particle Accelerator Conference*, pp. 169–173, May 2005.

[11] E. A. Rose, D. A. Dalmas, J. N. Downing, and R. D. Temple, "Testing pulse forming networks with darht accelerator cells," in *PPPS-2001 Pulsed Power Plasma Science 2001. 28th IEEE International Conference on Plasma Science and 13th IEEE International Pulsed Power Conference. Digest of Papers (Cat. No.01CH37251)*, vol. 2, pp. 1700–1703 vol.2, June 2001.

[12] C. J. Martin, *J. C. Martin on Pulsed Power*, vol. 3. Springer-Verlag New York, 2013.

[13] H. Bluhm, *Pulsed Power Systems Principals and Applications.* Verlag Berlin Heidelberg, Germany: Springer, 2006.

[14] A. Bouwers and P. Cath, "The maximum electric field strength for several simple electrode configurations," *Philips Technical Review*, vol. 6, no. 9, pp. 270–278, 1941.

[15] M. H. Samimi, A. Mahari, M. A. Farahnakian, and H. Mohseni, "The rogowski coil principles and applications: A review," *IEEE Sensors Journal*, vol. 15, pp. 651–658, Feb 2015.

[16] M. Argüeso, G. Robles, and J. Sanz, "Measurement of high frequency currents with a rogowski coil," *Rev. Sci. Instrum*, vol. 76, no. 6, pp. 065107–1, 2005.

[17] J. M. Taccetti, D. T. Westley, J. B. Johnson, and P. Flores, "Darht axis 1 compensation can d-dot calibration," tech. rep., 2017. Prepared for :.

[18] C. A. Ekdahl, "Voltage and current sensors for a high-density z-pinch experiment," *Review of Scientific Instruments*, vol. 51, no. 12, pp. 1645–1648, 1980.

[19] "Maxwell 18," 2018.

[20] O. Milton, "Pulsed flashover of insulators in vacuum," *IEEE Transactions on Electrical Insulation*, vol. EI-7, pp. 9–15, March 1972.

[21] P. W. Smith, *Transient electronics: pulsed circuit technology.* John Wiley & Sons, 2011.

[22] G. Schaefer, M. Kristiansen, and A. H. Guenther, *Gas discharge closing switches*, vol. 2. Springer Science & Business Media, 2013.

[23] "Goodfellow material information." `http://www.goodfellow.com/E/Polystyrene-Cross-linked.html`. Accessed: 2018-03-16.

[24] Dielectric Sciences, inc., *Pulse Cable*, 6 1981. http://dielectricsciences.thomasnet.com/Asset/2077.pdf.